

1 Quantifying the Impact of Modeling Fidelity on Different 2 Substructure Concepts - Part II: Code-to-Code Comparison in 3 Realistic Environmental Conditions

4 Francesco Papi¹, Giancarlo Troise², Robert Behrens de Luna³, Joseph Saverin³, Sebastian Perez-Becker³,
5 David Marten³, Marie-Laure Ducasse⁴, Alessandro Bianchini¹

6 ¹Department of Industrial Engineering, University of Florence, Firenze, 50139, Italy

7 ²Seapower srl, Naples, 80121, Italy

8 ³Hermann Föttinger Institute, Technical University of Berlin, Berlin, 10623, Germany

9 ⁴Saipem S.A., 1/7 Avenue San Fernando, 78884 Saint Quentin Yvelines cedex, France

10 *Correspondence to:* A. Bianchini (alessandro.bianchini@unifi.it) or F. Papi (fr.papi@unifi.it)

11 **Abstract.** Floating offshore wind is widely considered as a promising technology to harvest renewable energy in deep ocean
12 waters and increase clean energy generation offshore. While evolving quickly from a technological point of view, Floating
13 Offshore Wind Turbines (FOWTs) are challenging, as their performance and loads are governed by complex dynamics that are
14 a result of the coupled influence of wind, waves, and currents on the structures. Many open challenges therefore still exist,
15 especially from a modeling perspective. This study contributes to the understanding of the impact of modeling differences on
16 FOWT loads by comparing three FOWT simulation codes, QBlade-Ocean, OpenFAST, and DeepLines Wind[®] and three
17 substructure designs, a semi-submersible, a spar-buoy, and the two-part concept Hexafloat in realistic environmental conditions.
18 This extensive comparison represents one of the main outcomes of the H2020 project FLOATECH. In accordance with
19 international standards for FOWT certification, multiple design situations are compared, including operation in normal power
20 production and parked conditions. Results show that the compared codes agree well in the prediction of the system dynamics,
21 regardless of the fidelity of the underlying modeling theories. Some differences between the codes emerged however in the
22 analysis of fatigue loads, where, contrary to extreme loads, specific trends can be noted. With respect to QBlade-Ocean,
23 OpenFAST was found to overestimate lifetime damage equivalent loads up to 14%. DeepLines Wind[®], on the other hand,
24 underestimated lifetime fatigue loads by up to 13.5%. Regardless of the model and FOWT design however, differences in fatigue
25 loads are larger for tower base loads than for blade root loads, due to the larger influence substructure dynamics have on these
26 loads.

27 1 Introduction

28 In recent years industrial and academic interest around floating offshore wind energy has been increasing, thanks to its promise
29 to foster wind energy harvesting in offshore areas previously inaccessible with bottom-fixed wind turbines. To fully exploit the
30 advantages of this technology, ever larger and more flexible offshore turbines are being developed and deployed. These systems
31 are challenging to model, as their dynamics are governed by the coupled influence of aerodynamics, hydrodynamics, control,

32 and moorings. As an additional complexity, with large and flexible turbine rotors, aeroelastic coupling also plays an important
33 role. Many of the industry’s work-horse simulation codes have been developed with smaller, more rigid, bottom-fixed rotors in
34 mind and rely on engineering models, sometimes empirically derived, to model the relevant physical phenomena. In this context,
35 a real need for verification and validation of these tools exists. Several efforts, past and present, have been put into verification
36 and validation of offshore simulation codes. Notable examples being the Offshore Code Comparison (“OC” in short) programs
37 promoted by the International Energy Agency (IEA), OC3, OC4, OC5, OC6 (Jonkman and Musial, 2010; Robertson et al.,
38 2014b, 2017; Bergua and et. al., 2023) and the on-going OC7. Throughout the OC- projects, offshore codes have been compared
39 against other codes, and against wave-tank experiments. Especially OC4 and OC5 have helped highlight deficiencies in low-
40 frequency hydrodynamic modeling of semi-submersible type platforms (Robertson et al., 2017) that have allowed the advance
41 of the state-of-the art in OC6 (Robertson et al., 2020; Wang et al., 2022). Most of these campaigns have found that even simplified
42 engineering tools are generally able to capture the aerodynamics of these systems well - at times better than expected, such as in
43 (Bergua and et. al., 2023) – when compared to higher-fidelity and more physically complete aerodynamic models. Throughout
44 these comparison studies however, a limited number of often simplified inflow conditions have been tested. On the other hand,
45 some authors have found some differences between modeling theories when the coupled system dynamics are put to the test. In
46 particular, Corniglian, (2022) found increased blade root fatigue loads when comparing Blade Element Momentum Theory
47 (BEMT) to a higher fidelity Lifting-Line Free Vortex Wake (LLFVW) method. Similar considerations were also drawn by other
48 authors such as (Boorsma et al., 2020; Perez-Becker et al., 2020) when comparing fatigue load predictions on onshore wind
49 turbines. In detail, Boorsma et al. (Boorsma et al., 2020) have linked the increase in fatigue loads to increased 1P load variation,
50 while Perez-Becker et al. (Perez-Becker et al., 2020) have found that even small differences in aerodynamic modeling can lead
51 to different controller reactions, influencing overall loading and highlighting the importance of accurately modeling the entire
52 coupled dynamics of the system. In the case of FOWTs, dynamics are even more complex as the turbine moves in response and
53 in reaction to the incoming wind and wave variations. This introduces additional inertial and gravitational loading on many
54 structural components (Jonkman and Matha, 2011). Thus, differences in rotor loading may influence the response of the system,
55 indirectly influencing other component loads and amplifying the differences between the models.

56 The current study contributes to the field by presenting the outcomes of an extensive code-to-code comparison considering
57 realistic environmental conditions and three different floating substructure designs. Environmental conditions from an existing
58 European site are obtained using the procedure described in (Papi et al., 2022c) to obtain realistic distributions of wind speed,
59 significant wave height, peak spectral period and wind-wave misalignment. The three test-cases - a spar-buoy, a semi-
60 submersible and the innovative two-part floater concept; Hexafloat, recently proposed by Saipem - are simulated in a variety of
61 Design Load Cases (DLCs), including both power-production and parked conditions, as well as wind gusts. The test-cases are
62 simulated using three offshore codes, OpenFAST, DeepLines Wind and QBlade-Ocean, which was recently extended to enable
63 offshore simulations within the Horizon 2020 project FLOATECH. The latter code includes higher-fidelity modeling features
64 such as LLFVW wake aerodynamics and explicit buoyancy calculation, as illustrated in (Behrens De Luna et al., 2023).

65 The predicted dynamics are compared in terms of extreme loads, fatigue loads and statistics. Time series are also compared in
66 detail to give more insight into the differences in dynamics. The entire input conditions and compared datasets are available
67 open-access and can act as validation databases for other offshore codes or as a benchmark for future modeling improvements.
68 An extensive comparison, involving three different models with different substructure designs, three different numerical codes
69 and multiple DLCs that include hundreds of simulations is an important point of novelty of this study and does not come without
70 challenges. In fact, comparing coupled simulations that are aero-hydro-servo-elastic in nature such as in this study makes
71 isolating the potential sources of any differences challenging. Nonetheless, it offers the unique opportunity of evaluating the
72 trade-off between computational time and accuracy of the modeling theories in terms of their impact on the final design load
73 predictions in a realistic scenario. It also allows one to highlight user-bias in the set-up of FOWT simulations. In this view, some
74 critical aspects to consider during model set-up, that lead to significant differences in ultimate and fatigue loads in the compared
75 models such as structural damping ratios and control strategy are discussed in detail. Ultimately, the objective of this work is to
76 provide wind turbine modelers and practitioners with a quantitative indication of the impact that model fidelity has on FOWT
77 design loads and provide guidance in the selection of the most suitable approach for each task at hand.
78 This paper is organized as follows: In Sect. 2 the procedure required to set up the code-to-code comparison that is presented
79 herein is detailed, starting from environmental conditions and continuing with DLC definition, test-case selection, and data post-
80 processing. In Sect. 3 some details regarding the modeling theories underpinning the compared tools are given. In Sect. 4 the
81 main results are presented, starting from a general statistical comparison of key metrics, and then moving to the comparison of
82 design-driving extreme and fatigue loads. The principal results are discussed, and the conclusions drawn in Sect.5

83 **2 A Procedure for Code-to-Code Comparison of FOWTs in Realistic Environmental Conditions**

84 The set-up of a design load calculation of a FOWT is a complex task on its own. Expertise is required in the selection and set-
85 up of relevant DLCs in compliance with the various international standards (International Electrotechnical Commission, 2019a;
86 DNVGL, 2016). In the case of FOWTs, expertise is also required in the selection of environmental conditions to use, which are
87 site dependent. Finally, a full load calculation can produce thousands of hours of time series data, and data processing techniques
88 are required to make it more manageable and useful for the design process. In the context of this study, all these aspects will be
89 briefly presented as they have already been touched upon in two publications by the authors (Papi et al., 2022c; Papi and
90 Bianchini, 2023), that will be referenced later on in this Section where appropriate.

91 **2.1 European Met-Ocean Conditions**

92 Design classes are not currently prescribed for any type of offshore wind turbine as they are for onshore wind turbines, in favor
93 of standardization. Although the need for such standardization is acknowledged and encouraged in the DNVGL-SST-0119
94 design standard (DNVGL, 2018), the designer is currently required to verify the turbine and substructure combination of choice
95 for specific installation sites. As discussed in the following Sections, standards require the definition of specific wind conditions,

96 normally grouped in “models” such as the Normal Turbulence Model (NTM), and sea condition, generally grouped in “sea
97 states”. Some databases containing such met-ocean data can be found in previous work – for a comprehensive literature review
98 see (Papi and Bianchini, 2023) – however if we restrict our research to Europe, we did not find met-ocean conditions that were
99 completely suitable for this analysis. In fact, although conditions for some reference European sites can be found in the open
100 literature, such as in (Li et al., 2015), specific environmental contours are required to perform the ultimate load calculations
101 according to the prescriptions of International Standards. Therefore, an open-source procedure to obtain and prepare long-term
102 environmental data so it can be used in a design load calculation of an offshore wind turbine was developed. The procedure that
103 is detailed in (Papi et al., 2022c) and is available open-access for others to use and improve upon (10.5281/zenodo.6972014). A
104 highlight of the procedure is the fact that the statistical description of the installation site also includes wind-wave misalignment,
105 which has been shown to have a significant effect on loading (Stewart, 2016).

106 Data is obtained from the Copernicus re-analysis database ERA5. Environmental data is available on a 30x30 km grid, therefore
107 the procedure can be applied to a generic world-wide offshore site. In this study, hourly records of wind speed, wind direction,
108 significant wave height, wave direction and peak spectral period from 1979 to 2000 for a site located west of the Scottish island
109 of Barra are used. This location was chosen because of its particularly harsh environment, expected to increase non-linearities
110 and differences in the examined models, and because it is also used in other EU-funded projects such as LifeS50+ (Antonia
111 Krieger et al., 2015) and CoreWind (Vigara et al., 2020). Although more research would be needed to properly support this
112 claim, due to the severity of the considered met-ocean conditions, it is reasonable to believe that any differences between the
113 codes represent an upper limit, and smaller differences are likely to be found in less demanding conditions.

114 The open-source Python tool Virocon (Haselsteiner et al., 2019) is leveraged to build a joint probabilistic model of the dataset,
115 able to describe the long-term probability of the four environmental variables that are considered: wind speed (U_w), significant
116 wave height (H_S), peak spectral period (T_p) and wind-wave misalignment (M_{ww}). The model is then used to find the most likely
117 combination of H_S and T_p for a given U_w , defining the Normal Sea State (NSS), and to define environmental contours: extreme
118 conditions with 50-year recurrence period that are used to define the Extreme Sea State (ESS) and the Severe Sea State (SSS).
119 More details on how these sea states are defined are summarized in (Papi et al., 2022c), while information on environmental
120 contours and their applications to offshore wind turbines can be found in (Haselsteiner et al., 2020, 2021; Valamanesh et al.,
121 2015).

122 **2.2 DLC Selection and Simulation Conditions**

123 Code-to-code comparisons in a variety of environmental conditions are performed in this study. As such, simulations in various
124 met-ocean conditions are performed. The specific combination of met-ocean condition and operating condition is a Design Load
125 Case (DLC). In this study normal operating conditions and parked DLCs are simulated, as shown in Table 1. , While this
126 paragraph contains a general overview of the selected DLCs, a more detailed explanation of the selection process can be found
127 in the FLOATECH project deliverables (Papi et al., 2022a, b), and in (Papi and Bianchini, 2023). To obtain representative
128 ultimate loads, operation in extreme turbulence (DLC 1.3), in severe seas (DLC 1.6) and during an extreme operating gust with

direction change (DLC 1.4) are considered. In these load cases, wind and waves are considered aligned as a worst case scenario, in compliance with international standard prescriptions (International Electrotechnical Commission, 2019b). In DLCs where the turbine is parked during one year (DLC 6.3) and fifty years extreme environmental conditions, with (DLC 6.2) and without (DLC 6.1) grid loss, a $\mp 30^\circ$ wind-wave misalignment is also considered. All ultimate load DLCs simulations are one hour long, with the exception of DLC 1.4, where simulations are 10 minutes long. In this DLC, interest is put on the extreme loads caused by the transient wind gust. As such, these simulations can be shortened without loss of relevant information. Moreover, multiple turbulent seeds and yaw misalignments are considered within each DLC. For fatigue loads, normal operation in normal inflow and sea conditions (DLC 1.2) is considered. In this DLC, in accordance with indications coming from design standards (International Electrotechnical Commission, 2019a), that require the full design space to be explored, multiple sea states are examined, including multiple combinations of the four environmental variables. Therefore, the design space is divided into bins, and at least one model evaluation for each bin is required. To keep the number of simulations manageable in the context of a code-to-code comparison endeavor, two strategies to reduce the number of required model evaluations are adopted. Both strategies were proposed in (Stewart, 2016); the first is the “probability sorting method”, where the least likely bins are discarded as these conditions are unlikely and are expected to have little impact on fatigue loads. In this study the most likely bins, ensuring a total combined probability of 90% are kept in the analysis. The second strategy is bin coarsening, in which the width of the bins is increased, thereby reducing their number. As discussed in (Papi and Bianchini, 2023), by combining the two strategies a relatively manageable number of bins is obtained: 252. For each bin two half-hour simulations are performed with different yaw misalignments. The half-hour simulation length differs from the more commonly used one or three-hour simulation lengths. The rationale for such long simulations is to allow for enough time for low-frequency response, typical of FOWT systems, to build-up. Existing research (Stewart, 2016) however, indicates that the total time that is simulated within each environmental bin is the most important factor for fatigue-load estimation, rather than the length of each simulation. Moreover, based on the results in (Stewart, 2016), increasing simulation time beyond half-hour for each environmental bin does not appear to yield improved fatigue estimations in most cases. Therefore, considering the comparative nature of the study, two half-hour simulation for each environmental bin were considered sufficient for fatigue load comparison.

153

154 **Table 1: DLCs used in this study. Normal operating conditions in various sea states and turbulence levels in DLCs 1.2 to 1.6 for the**
 155 **evaluation of fatigue (F) and ultimate (U) loads. In DLCs 6.1 to 6.3 the FOWTs are parked in extreme conditions. In DLC 6.2 a grid**
 156 **loss scenario is modelled, and thus multiple values of yaw-error are considered. Acronyms and abbreviations are described in**
 157 **nomenclature list.**

DLC	wind		waves			dur. [s]	seeds/ws	yaw	n° ws	sims	type	
	model	speed	model	height	period							dir.
1.2	NTM	$V_{in}-V_{out}$	NSS	-	-	MUL	1800	1	0, 10°	11	504	F
1.3	ETM	$V_{in}-V_{out}$	NSS	$E[H_S V_{hub}]$	$E[T_P H_S]$	COD	1800	9	0, ∓ 10	11	99	U
1.4	ECD	$V_r \mp 2$ m/s	NSS	$E[H_S V_{hub}]$	$E[T_P H_S]$	COD	600	-	0	6	12	U

1.6	NTM	$V_{in}-V_{out}$	SSS	H_s , SSS	$E[T_P H_S]$	COD	3600	9	0, ∓ 10	11	99	U
6.1	EWM50	V_{50}	ESS	H_{S50}	$E[T_P H_S]$	$0^\circ, \mp 30^\circ$	3600	2	0, ∓ 10	1	12	U
6.2	EWM50	V_{50}	ESS	H_{S50}	$E[T_P H_S]$	$0^\circ, \mp 30^\circ$	3600	2	0,45,90 135,180	6	12	U
6.3	EWM1	V_1	ESS	H_{S1}	$E[T_P H_S]$	$0^\circ, 30^\circ$	3600	2	0, ∓ 20	1	12	U

158

159

160

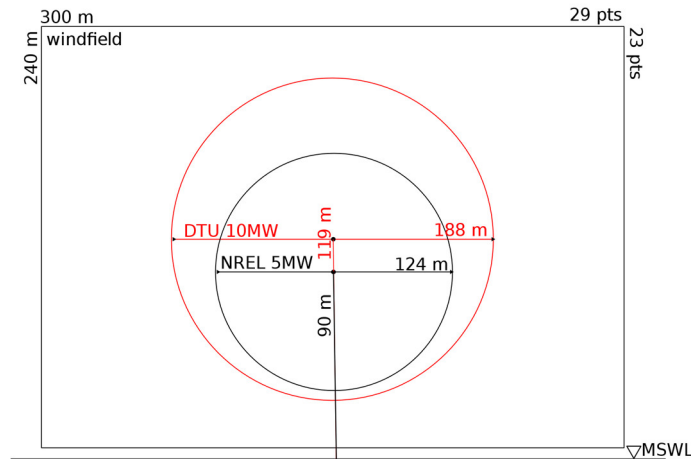
161

162

163

164

To ensure a fair comparison between the codes an attempt was made to match environmental inputs as well as possible in the numerical models. The wave time series are generated in DeepLines and then imported in OpenFAST and QBlade, while the wind fields are generated by each participating institution using the same TurbSim (Jonkman, 2014) settings. The same wind fields are used in all three test cases, as if they were installed in the same site, regardless of the rotor size used. Therefore, the larger 10MW rotor defines the overall size of the wind field. A schematic representation of the wind fields is shown in Fig. 1.



165

166

167

Figure 1: Schematic illustration of the wind field dimensions as used in this study with respect to the NREL 5MW and DTU 10MW rotors. The same wind fields are used on all three test-cases regardless of rotor size.

168

2.3 Considered FOWT Designs

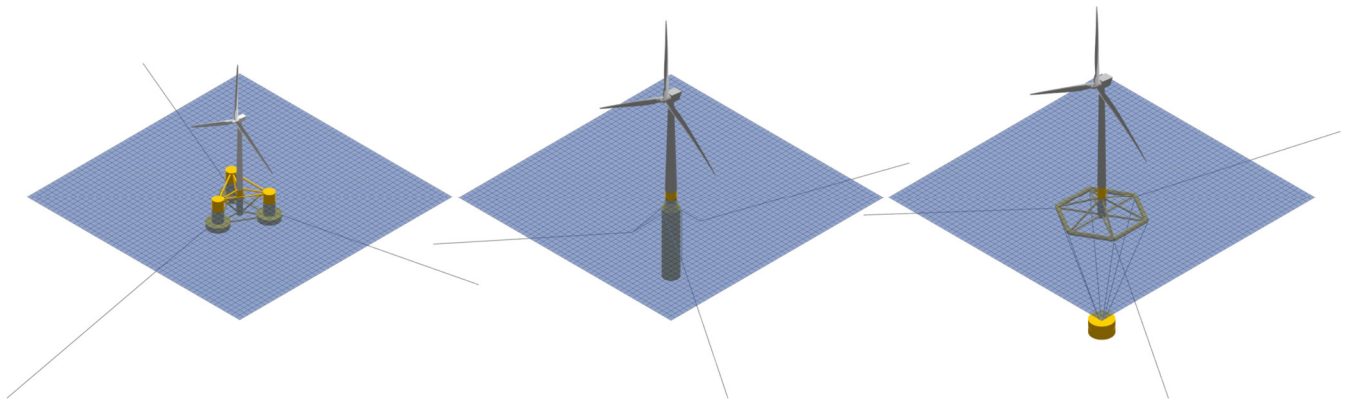
169

170

171

172

For the sake of generality and completeness of the analysis three floating turbine concepts are analyzed. Each test case features a different floating platform concept, namely a semi-submersible, a spar-buoy and Hexafloat. The three concepts are all derived from those in (Perez-Becker et al., 2022; Behrens De Luna et al., 2023), where some calibration was required to properly align the models with the experiments. The main characteristics of the three test-cases are detailed in the following.



173
174 **Figure 2: Illustration of the examined numerical models in QBlade-Ocean. From left to right: NREL 5MW OC4, DTU 10MW Softwind**
175 **and DTU 10MW Hexafloat.**

176
177 **2.3.1 NREL 5MW OC4 DeepCwind**

178 The NREL 5MW OC4 semi-submersible FOWT (hereafter OC4) is an open-access turbine model defined in (Robertson et al.,
179 2014a), upon which many code-to-code comparison exercises are based (Robertson et al., 2014b, 2017). It makes use of the
180 NREL 5MW RWT rotor (Jonkman et al., 2009), representative of a utility-scale multi-MW rotor. The rotor is mounted on the
181 DeepCwind semisubmersible floating platform. The platform was developed with the aim of generating test data for use in the
182 validation of FOWT modeling tools.

183 The same tower design that was developed for use on the OC3-Hywind spar platform (Jonkman, 2010) is used. The semi-
184 submersible floater consists of a main central column connected to the tower and three side columns spaced 120° apart. The
185 offset columns are larger at the base, acting like heave plates to control the vertical motion of the FOWT and are connected
186 together through a series of braces. A catenary mooring system is used. Three 120° lines are used to anchor the turbine to the
187 seabed with one mooring line pointing directly upwind and the other two downwind.

188 **2.3.2 DTU 10MW Softwind**

189 The DTU 10 MW Softwind spar FOWT (hereafter Softwind) is a 1:40 scale floating platform designed by École Centrale de
190 Nantes to develop, demonstrate, and validate a Software in the Loop (SiL) approach whereby an actuator is used to simulate the
191 aerodynamic forcing at model scale in place of a scaled rotor. The model and experiments are described in (Arnal, 2020). The
192 rotor nacelle assembly (RNA) is described in (Bak et al., 2013). With respect to the models used in (Behrens De Luna et al.,
193 2023) that mimic the characteristics of the experiments (Arnal, 2020), some changes were implemented to increase the robustness
194 of the numerical simulations when using the realistic met-ocean conditions considered in this work. Namely, the tower was

195 stiffened, moving to a stiff-stiff design to avoid wave and 3P tower resonance. The tower designed by Olav-Olsen¹ in the
196 LifeS50+ project for the OO-Star floater is used (Borg, 2015; Yu et al., 2018). Notably this tower is heavier than the one used
197 in the Softwind test campaign. The mass distribution in the floater is also changed. In order to have a realistic mass distribution
198 and inertial properties, we hypothesized the use of high-density ballast in the spar body, thus lowering the Center of Gravity
199 (CoG) with respect to the scaled model used in the experiments, which housed control electronics and batteries within the buoy.
200 The mass of the floater is also lowered by approximately 2% to compensate for the heavier tower and maintain approximately
201 the same draft. Furthermore, lowering the CoG lowers the platform pitch natural period, allowing for the use of a faster controller,
202 as explained in Sect. 3.3. The specific changes are detailed in (Papi et al., 2022a). This modified floater design is not intended
203 to be built and is only meant for numerical comparisons using a realistic design that is also numerically stable. These changes
204 are therefore deemed appropriate for the goal of this study.

205 In DeepLines, after unsuccessful initial attempts to align the model to QBlade and OpenFAST, and, in an initial phase, to the
206 Softwind experiments (Arnal, 2020), a different tuning approach was employed for the hydrodynamics of the model. In
207 particular, the pitch and roll inertias of the floater were decreased to better align the respective natural frequencies in free decay
208 tests, and additional added mass on the spar buoy was introduced through Morison's equation to improve the agreement during
209 surge free-decay tests. Lastly, mooring line tension was lowered to better align with the experimental data. A full description of
210 the differences can be found in (Papi et al., 2023).

211 **2.3.3 DTU 10MW Hexafloat**

212 The DTU 10MW Hexafloat FOWT consists of the DTU 10MW RWT mounted to the Hexafloat floater concept proposed by
213 Saipem. As shown in Fig. 2, the substructure consists of a floater made of relatively slender steel braces connected to a
214 counterweight by six tendons. This floater configuration did not require changes to the tower design and therefore the standard
215 onshore tower of the DTU 10MW RWT (Bak et al., 2013) is used. This model is in effect identical to the one used and described
216 in (Perez-Becker et al., 2022; Behrens De Luna et al., 2023)

217 **2.4 Post-Processing and Data Management**

218 The raw time series data obtained for the three models is post-processed using open-source tools, namely MLife (Hayman, 2012)
219 and MExtremes (Buhl, 2015) developed by NREL. The main sensors that are compared in the study are shown in Tab. 1 and
220 consist of blade root and tower base bending moments, mooring line fairlead tensions, nacelle fore-aft acceleration, control
221 signals and platform motions. Some of these sensors act like a proxy to compare the influence of various physical phenomena
222 on loads, such as nacelle acceleration that is used to gauge inertial loads on the tower and platform pitch that is used as indication

¹ The OO-Star Wind Floater has been developed by Dr. Techn. Olav Olsen (OO) since 2010 and is the property OpenFAST Floating Wind Solutions AS. OO has approved that the public model from LifeS50+ can be used for the research activities within FLOATECH. The model shall not be used for other purposes unless it is explicitly approved by OO.

223 of gravitational tower loading. The mechanisms that relate platform motions and substructure loading are discussed in (Robertson
224 and Jonkman, 2011; Papi and Bianchini, 2022) and will only briefly be explained throughout this work where necessary.
225 MLife is used to compute Damage Equivalent Loads (DELs). DELs are the cyclic load amplitudes that cause the same fatigue
226 damage to the structure over a certain number of cycles as the time series of a given load sensor. The Palmgren-Miner linear
227 damage accumulation hypothesis is used to derive DELs, which can therefore only be considered representative equivalent loads
228 if this hypothesis is valid. In this study zero-mean DELs are considered, and thus the mean of each loading cycle is disregarded.
229 1Hz DELs give the equivalent damage during one simulation, while lifetime DELs represent the equivalent damage over the
230 entire lifetime of the turbine. They can be conceptually thought of as a combination of 1Hz DELs weighted by their respective
231 probability of occurrence, which in this case is a distribution that depends on the four environmental variables defined in Sect.
232 2.1. As shown in Tab. 1, only the simulations in DCL 1.2 are used to compute DELs.
233 MExtremes is used to compute ultimate loads on the structure. In this case, DLCs 1.3, 1.4, 1.6, 6.1, 6.2 and 6.3 are used. To
234 obtain a conservative estimate of ultimate loads in accordance with IEC 61400-1 annex I (International Electrotechnical
235 Commission, 2019a), an averaging approach is used when computing ultimate loads, as explained in (Buhl, 2015).

236

Table 1: Sensors considered in the analysis.

Sensor	OpenFAST ref. sys.	Name	Type
Blade root in-plane/out-of-plane bending moment	Coned CS c	B# M _x / B# M _y	F/U
Tower base fore-aft/side-side bending moment	Tower base CS t	TB M _y /TB M _x	F/U
Mooring line fairlead tensions	-	T ML#	F/U
Nacelle fore-aft acceleration	Tower top CS p	Nac. TAx	U
Control signals (blade pitch, gen. torque, rotor speed)	-	θ, τ, Ω	-
Platform motions (computed @SWL)	Platform CS	surge, sway, pitch, etc...	-

237 **3 Methods**

238 This work leverages some of the authors' past experience and as such many of the same modeling techniques as described in
239 (Behrens De Luna et al., 2023) are used, where a more complete description of the employed methods can be found. Three
240 distinct numerical tools are used in this code-to-code comparison: OpenFAST v3.0, DeepLines Wind[®] and QBlade-Ocean. The
241 tools have been compared to experimental results on scaled models and have shown, after adequate model tuning, good ability
242 to capture the behavior of the different systems. The results of this modeling and validation effort are discussed in (Perez-Becker
243 et al., 2022; Behrens De Luna et al., 2023). The main numerical models in each code are described in this Section.

244 **3.1 Aerodynamic Models**

245 All the models compared herein use low- to medium-fidelity aerodynamic models. The blade aerodynamics are not explicitly
246 modeled. Instead, a series of 2D aerodynamic coefficients is used in their place. Corrections to account for 3D flow effects are

247 built into the aerodynamic coefficients for all the models. Moreover, Gonzalez’s variant of the Beddoes-Leishman dynamic stall
248 model (Leishman, 2016; Damiani and Hayman, 2019) is used in OpenFAST. In QBlade dynamic stall is modeled using Øye’s
249 model (Marten, 2020), while in DeepLines no unsteady airfoil aerodynamics are accounted for. The relative velocities acting
250 on the blades are determined by the wake model. A Dynamic Blade Element Momentum (DBEM) wake model is used in
251 OpenFAST and DeepLines, where the rotor is divided into a series of radial and azimuthal streamtubes and for each streamtube
252 a momentum balance is performed. More details on BEM models can be found in (Burton, 2001; Hansen, 2008), and details
253 regarding the specific DBEM model implemented in OpenFAST are in (Ning et al., 2015; Branlard et al., 2022). These models
254 have been the industry workhorse for decades and although very simple, they have been extended in time through the addition
255 of empirical sub-models and now fully qualify as engineering models. A higher-order Lifting Line Free Vortex Wake (LLFVW)
256 model is used in QBlade. Here, the wake is modeled as a series of vortex filaments. Wake nodes are advected downstream by
257 the incoming wind speed and the cumulative induction of all wake filaments. More details on these models and how they are
258 implemented in QBlade can be found in (Van Garrel, 2003; Marten et al., 2015). The same aerodynamic lift and drag tables are
259 used in all three codes for both aerodynamic models and correspond to the public definitions of the NREL 5MW and DTU
260 10MW rotors.

261 **3.2 Structural Models**

262 Structural dynamics are modeled with a modal-based linear superposition approach in OpenFAST through the submodule
263 ElastoDyn. One limitation is that blade torsion is not modeled in ElastoDyn. In QBlade and DeepLines on the other hand, a
264 higher fidelity finite-element approach is used, whereby the structural dynamics are modeled with a multi-body representation
265 that uses Euler-Bernoulli beam elements in a co-rotational formulation (Marten, 2020; Le Cunff et al., 2013). Within OpenFAST
266 a more sophisticated blade structural model exists that is able to account for blade torsion. Nonetheless, it was chosen to use
267 ElastoDyn in this study for two reasons. The first reason is to speed up the OpenFAST calculations, as ElastoDyn requires less
268 computational resources to run. The second reason is that by using a simpler structural model in OpenFAST, the impact of this
269 choice on the global dynamics and loads of the chosen floating systems can be evaluated.

270 **3.3 Control**

271 In all three models the ROSCO v2.4.1 open-source controller (Abbas et al., 2022) is used. This controller has been selected as it
272 is open-source and it includes an automatic tuning toolbox that can be used to determine the proportional and integral gains of
273 the blade pitch controller in a simple manner (Lenfest et al., 2020). A traditional $K\omega^2$ law is used for the torque controller below
274 rated wind speed. Above rated wind speed constant-torque control strategy is used. The pitch controller gains are tuned using
275 ROSCO controller’s automatic pitch-tuning routine based on the OpenFAST models of the two rotors. The controller includes
276 a nacelle-velocity feedback loop developed especially for FOWTs, with the objective of avoiding negative blade-pitch controller
277 damping that can occur in the case of FOWTs. However, this feature is not used in this study. The reason for this being that the
278 feature did not work for the DeepLines models, as the required nacelle velocity sensor was not available as a controller input in

279 this code. In order to have a fair comparison between all codes, we decided to disable this feature and instead tuned the pitch
 280 controller to have lower PI-feedback terms. The natural frequencies and damping ratios of the pitch controller used for the three
 281 models are shown in Table 2. For all three models the natural frequency of the blade pitch controller is set below the platform
 282 pitch natural frequency, mitigating possible controller-driven system instabilities. Despite this, a certain degree of blade pitch-
 283 induced platform motion is noted, especially in the Softwind test-case, at near-rated wind speeds. The phenomenon impacts
 284 QBlade simulations more than OpenFAST and DeepLines simulations. The reason for this difference is probably linked to slight
 285 differences in the aerodynamic models that cause different controller reactions, as explained in detail in Sect. 4.3.1.

286 In the OC4 model, a peak-shaving minimum pitch saturation schedule is considered. Peak shaving is used to reduce loads near
 287 rated wind speed by imposing a minimum pitch angle as a function of the low pass filtered wind speed at hub height, as explained
 288 in (Abbas et al., 2022). In this model the same settings are used as in the public example that can be found in the ROSCO
 289 repository.

290 In DLC 1.4 shut-downs are performed by overriding the blade pitch controller with a specified pitch to feather maneuver in each
 291 code. The pitch to feather maneuver is initiated 5 seconds after the wind gust peak, as if the controller was reacting to the
 292 detection of an extreme yaw error and the blades are pitched at a speed of 10 °/s. In DeepLines the pitch to feather maneuver is
 293 longer in duration due to a setup difference. In fact, a specific pitch rate during a pitch to feather override maneuver cannot be
 294 specified in DeepLines, which needs a start and end time of the operation. Therefore, depending on the initial blade pitch angle,
 295 which depends on the coupled simulation and is thus different for each turbulent seed and each code, this can result in different
 296 pitch rates.

297 **Table 2: Controller natural frequencies and damping ratios for the three test-cases.**

Model	Nat. $f(\omega)$	Damping ratio (β)
NREL 5MW OC4	0.2 [rad/s]	1 [-]
DTU 10MW Softwind	0.14 [rad/s]	1 [-]
DTU 10MW Hexafloat	0.114 [rad/s]	1 [-]

298 3.4 Hydrodynamics

299 For the OC4 and Softwind designs a Potential flow with Morison Drag (PFMD) approach is used in both OpenFAST and QBlade,
 300 whereby hydrodynamics are modeled by combining a potential flow solution with quadratic drag computed with Morison’s
 301 equation (ME). Full difference-frequency Quadratic Transfer Functions (QTFs) are used in both QBlade and OpenFAST in the
 302 OC4 design. They were computed and provided for this geometry by ECN using NEMOH (Kurnia et al., 2022), a potential flow
 303 hydrodynamic solver developed by ECN. On the Softwind design, quadratic hydrodynamic excitation forces are included with
 304 Newman’s approximation (Faltinsen, 1993). The same hydrodynamic coefficients are used for each design in all three models.
 305 Buoyancy is modeled differently in the three codes: QBlade and DeepLines model this force explicitly. The spar structure is
 306 divided into a series of cylindrical sections and buoyancy forces are discretely applied. OpenFAST on the other hand models
 307 buoyancy force as constant term and a linear stiffness matrix to include the contributions of buoyancy to the restoring forces on

308 the platform. Moreover, QBlade and DeepLines are able to model Wheeler wave stretching, which may introduce additional
309 non-linear forcing. In the Hexafloat model a different approach is used. In fact, the floater is made of relatively slender braces
310 that can be adequately modeled with a ME approach (Faltinsen, 1993). The same added mass and drag coefficients in both the
311 axial and transversal directions are used in DeepLines and QBlade, and the hydrodynamic forces predicted by the two codes
312 match well (Perez-Becker et al., 2022). The improvements implemented in QBlade to capture the slow-drift hydrodynamic forces
313 described in ((Behrens De Luna et al., 2023), Sect. 3.4), are not used in this study, and all three models share the same basic
314 hydrodynamic model, with the respective differences highlighted in this Section.

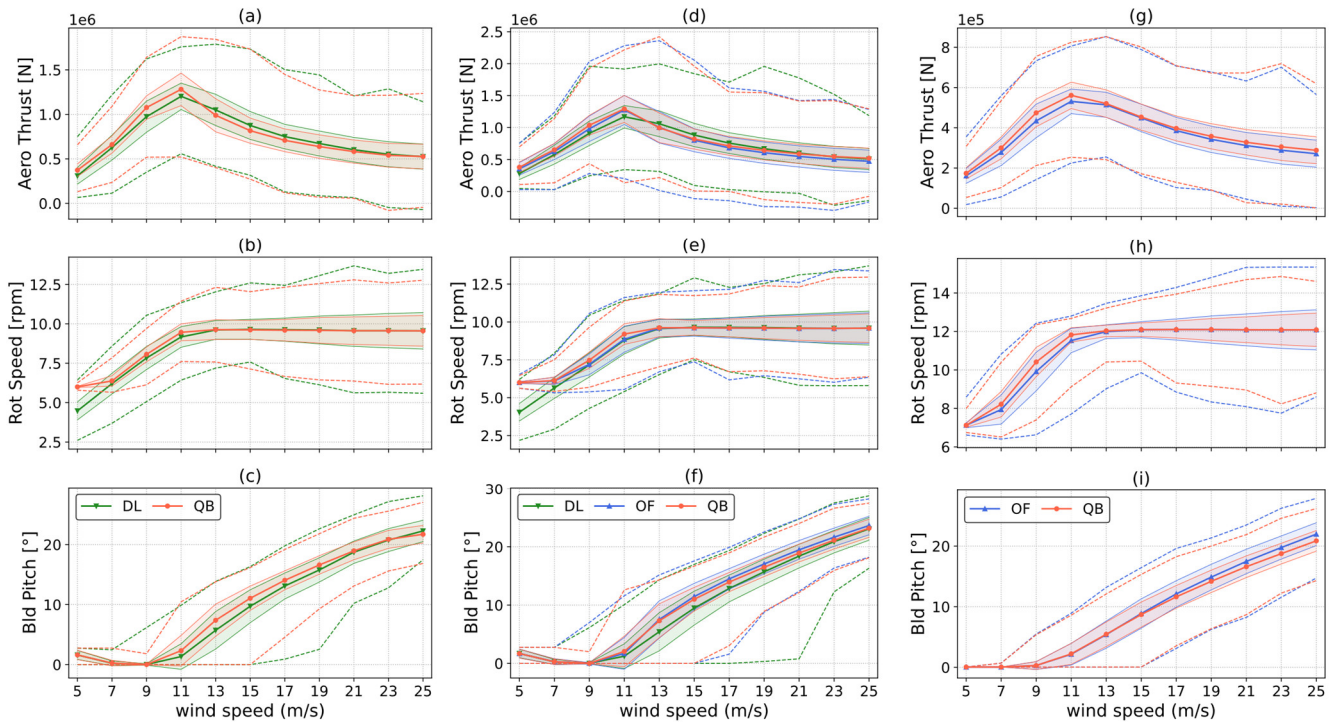
315 **4 Results**

316 In this Section the most relevant results are presented. General statistical information is presented first, followed by a selection
317 of ultimate loads recorded in DLCs 1.3 – 6.1 (Table 1) and a selection of lifetime DELs to compare fatigue load predictions. The
318 Softwind design is used as the design of choice in most cases as it features all three codes, and results from the other two designs
319 are also discussed when necessary. We were unable to complete all the simulations in all three codes in the comparison due to
320 numerical convergence issues. In particular, one out of sixteen simulations in DLC 6.2 in the Softwind model was not completed
321 in OpenFAST because of instabilities in the structural solver. Moreover, we were unable to complete all simulations in DLCs
322 1.2 (498/504), 1.3 (86/99), 6.1 (12/18), 6.2 (12/16) and 6.3 (12/18) in DeepLines. Similar issues are also present in the Hexafloat
323 model in DeepLines, where simulations did not converge in DLCs 1.2 (497/504), 6.1 (12/18), 6.2 (12/16) and 6.3 (12/18). The
324 cause of the incomplete runs can again be traced back to numerical instabilities in the solution. We chose not to attempt re-
325 running the simulations with a fine-tuning of the numerical solution scheme parameters because of budget and time constraints
326 within the project. Therefore, while not an inherent limitation of the code, this result is what could be achieved by a prepared
327 operator within the project timeline, which is also comparable to that of an industrial project. We were able to complete all the
328 simulations in QBlade. Results have shown good agreement between the codes in DLCs where the machine is operating, but
329 some discrepancies when the machine is parked. Moreover, generally larger differences in fatigue loads than in extreme loads
330 between the codes are noted.

331 **4.1 Statistical Comparison**

332 Figures 3 and 4 show a statistical comparison of selected operational sensors over the working range of the wind turbines. The
333 wind speed is extracted at 100 m above mean sea water level. The markers represent the mean values recorded in DLC 1.2, the
334 shaded area corresponds to twice the standard deviation of the signal for each wind speed and the dashed lines show the minimum
335 and maximum values recorded during the DLC 1.2 runs. Control sensors, often used to monitor the operation of the wind turbine,
336 are shown in Fig. 3. Although global trends are the same for all three codes in all three test-cases, some important differences
337 can be pointed out. With respect to QBlade, mean aerodynamic thrust is lower for DeepLines in the Softwind and Hexafloat test
338 cases at below rated wind speed and is also lower for OpenFAST in the OC4 test-case. In the case of the OC4 test-case, the

339 difference in thrust can, at least partially, be attributed to differences in rotor speed (Fig. 3 (h)). In fact, mean rotor speed is
 340 higher in QBlade, causing the rotor to operate at a higher tip speed ratio (TSR), leading to a higher thrust coefficient. Similar
 341 differences in this regard were noted also in previous comparisons between QBlade and OpenFAST (Perez-Becker et al., 2020).
 342 For the Softwind and Hexafloat test-cases (Figs. 3 (b, e)), less difference in rotor speed can be noted, and the difference in thrust
 343 is therefore more likely to be caused solely by differences in the aerodynamic models. The differences in aerodynamic modeling
 344 are also apparent when analyzing blade pitch statistics in Figs. 3 (c, f, i). In fact, while good agreement in mean values can be
 345 noted for QBlade and OpenFAST, mean blade pitch is lower for DeepLines through most of the wind speed range. In addition,
 346 the difference between maximum and minimum blade pitch angles is larger for DeepLines with respect to OpenFAST and
 347 QBlade. Moreover, as shown in Fig. 3 (b, e), minimum rotor speed is not enforced in DeepLines, and the rotor operates at lower
 348 rpm at cut-in in both the Hexafloat and Softwind test cases. The ROSCO controller that was used in this code-to-code comparison
 349 required recompiling to be used in DeepLines Wind because the blade pitch and twist angle conventions that are used in this
 350 code differ from those used in QBlade and OpenFAST and as a result, minimum rotor speed is not enforced in DeepLines. To
 351 the best of our knowledge, the controller is functionally identical to that used in OpenFAST and QBlade in all other aspects.
 352 This influences fatigue loads, especially edgewise and in-plane blade root bending moments, that are strongly dependent on
 353 cyclic gravitational loading. On the other hand, we can assume the influence of this discrepancy on extreme loads to be limited,
 354 as these loads are recorded at higher mean wind speeds.

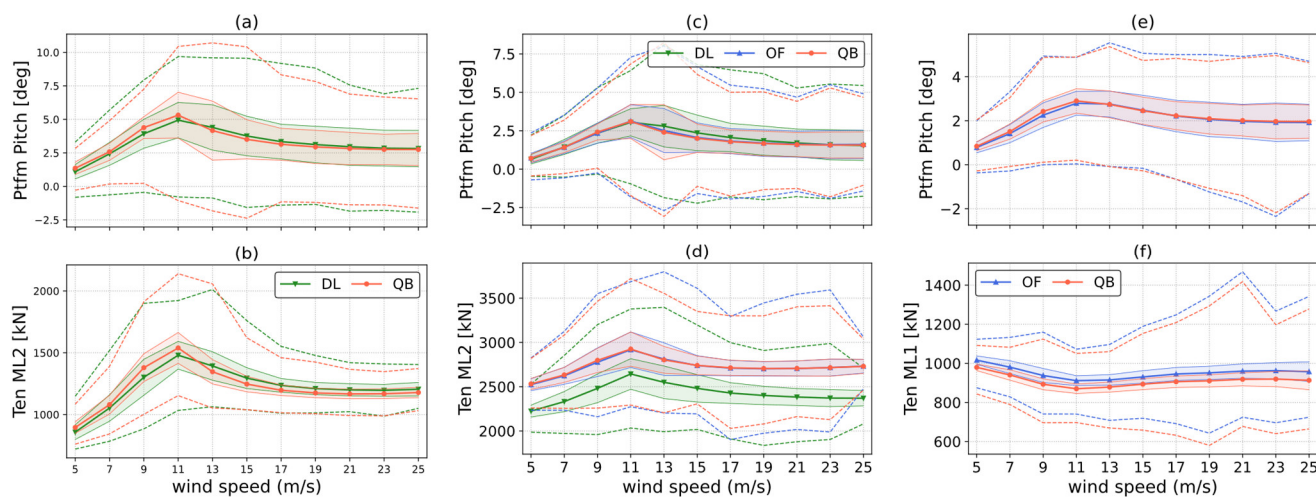


355

356 **Figure 3: Statistics of aerodynamic thrust (a, d, g), rotor speed (b, e, h) and blade pitch (c, f, i) as a function of mean wind speed**
 357 **recorded in DLC 1.2. Solid lines with markers represent mean values, shaded areas represent twice the recorded standard deviation,**

358 dashed lines for the minimum and maximum recorded values. DTU 10MW Hexafloat (a-c), DTU 10MW Softwind (d-f) and NREL
 359 5MW OC4 (g-i).

360 In Fig. 4, statistics of platform pitch and mooring line tension are shown. For the Softwind and Hexafloat test-case one of the
 361 two upwind mooring lines is chosen, while for the OC4 test-case the tension of the upwind mooring line is reported in Fig. 4 (f).
 362 As for the control sensors shown in Fig. 3, good general agreement can be seen for all three codes in all three test-cases. Platform
 363 pitch is remarkably similar in mean value, standard deviation, and minimum/maximum value for the OC4 test-case (Fig. 4 (e)),
 364 although higher standard deviation can be noted for wind speed near cut-in and cut-out in OpenFAST. This is interesting because
 365 a higher platform-pitch standard deviation indicates increased gravitational and inertial loading variations on the tower. Very
 366 good agreement between OpenFAST and QBlade is also shown in Fig. 4 (c). Despite platform pitch standard deviation being
 367 lower in QBlade for most wind speeds, at 13 m/s mean wind speed it is higher for QBlade. A similar trend can also be noted in
 368 Fig. 4 (a), where again the standard deviation of blade pitch is higher for QBlade at 11 m/s and 13 m/s mean wind speeds.
 369 Analyzing the time series of the various codes at these wind speeds reveals that the increased standard deviation in QBlade near
 370 rated is a result of blade pitch – platform pitch self-excitation. This phenomenon is discussed in detail in Sect. 4.3. Mooring line
 371 tensions are in good agreement in all three test-cases although some differences can be noted. The largest difference is shown in
 372 Fig. 4 (d), where a significant difference in mean tension can be noted between DeepLines and the other codes. Such difference
 373 is a result of different model tuning, as discussed in Sect. 2.3.2.

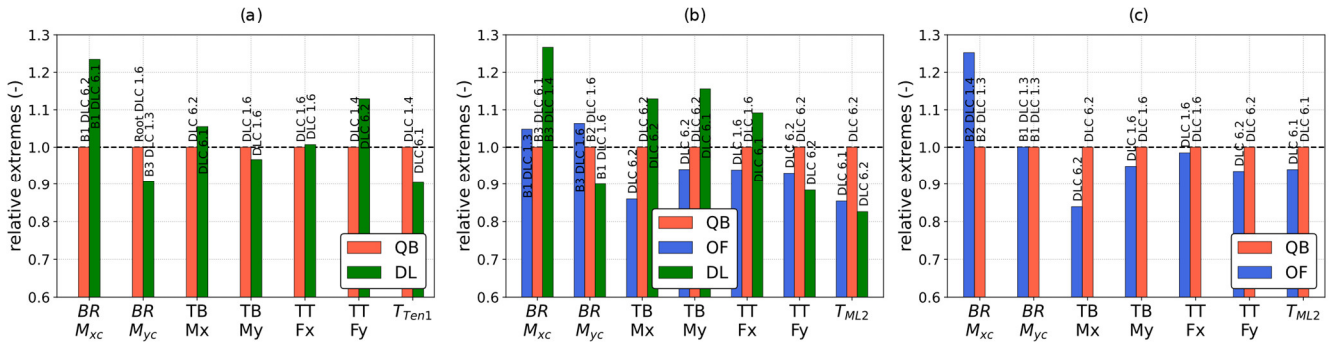


374
 375 **Figure 4: Statistics of platform pitch (a, c, e), upwind mooring line tension (b, f) and tendon tension (d) as a function of mean wind**
 376 **speed recorded in DLC 1.2. Solid lines with markers represent mean values, shaded areas represent twice the recorded standard**
 377 **deviation, dashed lines for the minimum and maximum recorded values. DTU 10MW Hexafloat (a-b), DTU 10MW Softwind (c-d) and**
 378 **NREL 5MW OC4 (e-f).**

379 4.2 Ultimate Loads

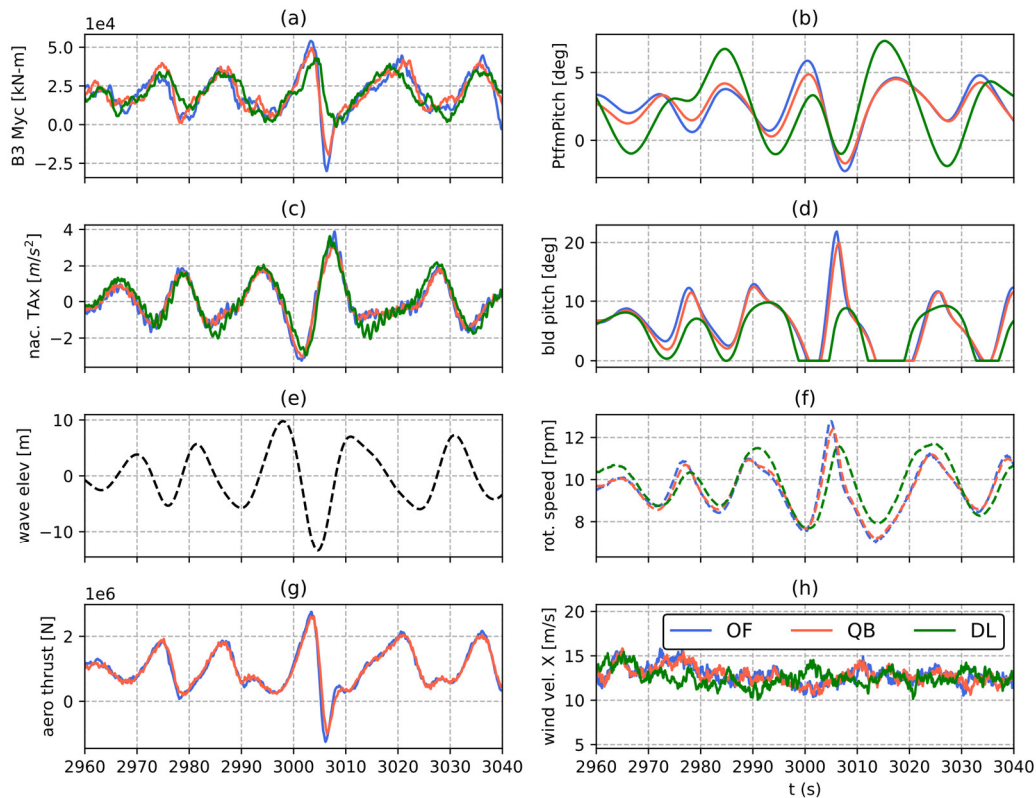
380 This Section presents the ultimate loads, computed with the maximum averaging method described in Sect. 2.4, for key selected
 381 load sensors. This Section is focused on understanding which phenomena and modeling differences may influence the prediction

382 of extreme loads. The analysis focuses on maximum extreme loads only, disregarding minimum loads to streamline the
 383 discussion. Minimum extreme loads are reported in Appendix A. In Fig. 5, the ratios of selected ultimate loads on the turbine
 384 with respect to the values obtained in QBlade, assumed here as benchmark, are shown. The DLCs in which the respective
 385 maximums are recorded are also reported for each of the bars in Fig. 5. For blade root bending moments, the maximum value
 386 recorded across the three blades is shown. Figure 5 also reports the blade where the peak load is recorded. Ultimate loads are
 387 recorded across all the DLCs, thus encompassing both power production and parked load cases, depending on the specific load
 388 sensor and FOWT design being examined. In the OC4 test case (Fig. 5 (c)) extreme loads are predicted in the same DLC in
 389 OpenFAST and QBlade, with the exception of blade root in-plane bending moment (BR M_{xc}). This FOWT design is the one
 390 where the best overall agreement between the compared codes was reached. In the Softwind and Hexafloat designs, extreme
 391 loads are recorded in different DLCs for some load sensors, as is the case for TT F_x for Softwind and BR M_{yc} for Hexafloat. In
 392 both cases extreme loads predicted across multiple DLCs are very close in magnitude, causing the ultimate extreme load to be
 393 predicted in different DLCs depending on the specific model's response.



394

395 **Figure 5: Selection of ultimate loads (maximum) recorded in the three simulation codes. (a) DTU 10MW Hexafloat, (b) DTU 10MW**
 396 **Softwind and (c) NREL 5MW OC4.**



397
 398 **Figure 6: Time series of out-of-plane root bending moment of blade 3 of the Softwind model in DLC 1.6, ($w_s = 11$ m/s, $H_s = 9$), where**
 399 **maximum bending moment is recorded for OpenFAST. From top to bottom: B#3 out-of-plane root bending moment (a), platform**
 400 **pitch (b), nacelle fore-aft acceleration (c), blade pitch (d), and wave height at platform reference position (e), rotor speed (f),**
 401 **aerodynamic thrust (not available in DeepLines outputs) (g), wind speed at hub height (h).**

402 4.2.1 Blade Root Extreme Loads

403 Regarding blade root bending moments, there is larger variation in BR Mxc ultimate load than BR Myc. BR Myc is much higher
 404 in magnitude than BR Mxc and thus has a greater influence on component design. Nonetheless, BR Mxc is approximately 23%
 405 higher on the Hexafloat test-case for DeepLines, and 27% higher in the Softwind test-case. Similarly, BR Mxc is approximately
 406 25% higher for OpenFAST in OC4. Out-of-plane blade root bending moments are in better agreement, DeepLines predicting
 407 10% lower loads than QBlade in the Hexafloat and Softwind test-cases, while OpenFAST and QBlade are much closer, the
 408 former being 5% higher in Softwind and nearly identical to QBlade in OC4.

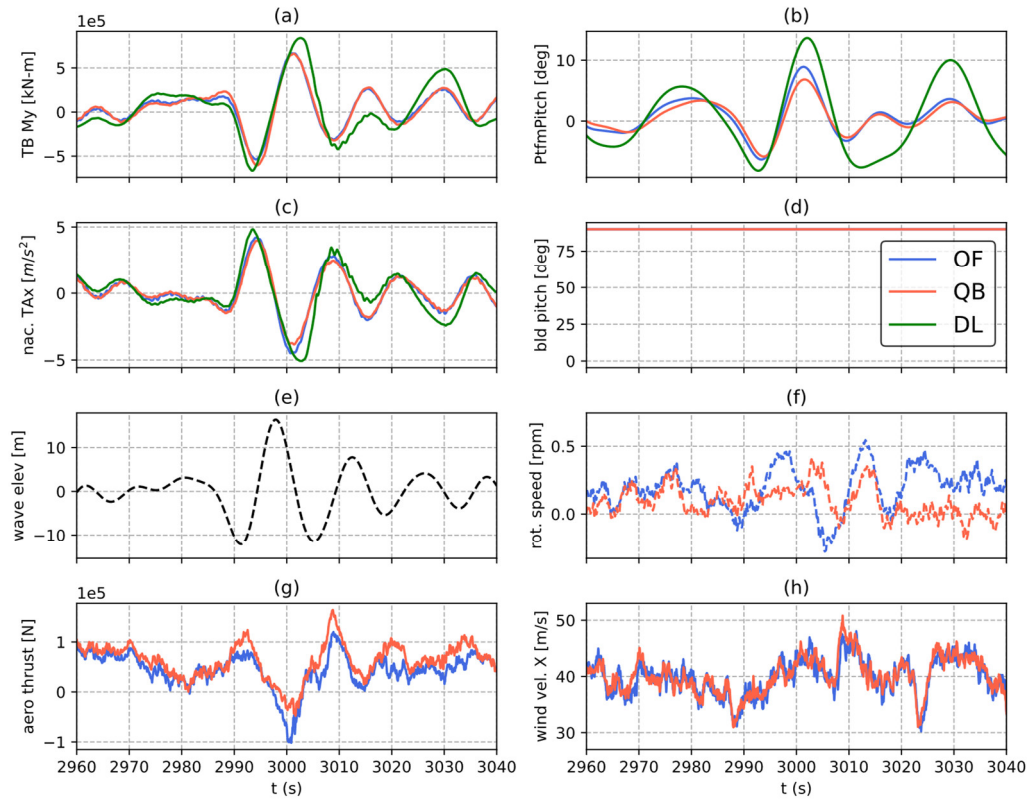
409 The out-of-plane blade root bending moments are mostly influenced by aerodynamic loading, as lift force is directed mostly out-
 410 of-plane. On a FOWT however, the coupled dynamics of the entire system influence these load sensors. This is demonstrated in
 411 Fig. 6, where the time series of multiple load sensors, including BR Myc, platform pitch, aerodynamic thrust and nacelle fore-
 412 aft acceleration are shown at the time instant where the maximum BR Myc in OpenFAST is recorded. When the load peak is
 413 recorded the wind speed is rising and is around the rated wind speed value. In addition, an extreme wave impacts the substructure.

414 The latter causes the FOWT to move, as shown in the platform pitch and nacelle fore-aft acceleration sensors time series. In turn
415 this causes large relative inflow variations on the rotor. As hydrodynamic forces cause the platform to swing forward, rotor thrust
416 increases causing BR Myc to peak. Due to the increase in relative inflow, rotor speed increases (Fig. 6 (d)) and the controller
417 reacts by aggressively pitching the blades, especially in QBlade and OpenFAST. While controller response depends on and
418 influences the global response of the system, one reason for the different controller reactions in DeepLines is the different wind
419 speed in this code (Fig. 6 (e)). In fact, the same wind fields are used in all three codes, but a time-shift is present in DeepLines
420 with respect to the other models due to differences in how the wind fields are imported. In fact, depending on the simulation
421 tool, wind fields are often shifted on import in order to make sure that the turbine is fully immersed in the wind field in case of
422 yaw misalignment. On the other hand, no such shift is present in the wave fields. Therefore, environmental inputs are out of sync
423 if OpenFAST and QBlade are compared to DeepLines. The increase in blade pitch is able to limit rotor speed overshoot but
424 causes a sudden decrease in rotor loading, which in turn is the cause of BR Myc reaching a local minimum shortly after peaking.
425 Therefore, platform motion influences BR Myc indirectly: not through variation in inertial and gravitational loads but through
426 variation in aerodynamic loading. In summary, even small differences in aspects such as input conditions, hydrodynamics,
427 aerodynamics, control, and overall set-up definition can influence ultimate loads through different system dynamic behavior.

428 **4.2.2 Tower Base Extreme Loads**

429 Shifting focus to tower base loads, fore-aft (TB My) are, similarly to blade root loads, greater in magnitude than side-side loads
430 (TB Mx) that will thus be treated briefly. Side-side tower base bending moment (TB Mx) ultimate load always occurs in parked
431 conditions for all three test-cases and all three design codes. Moreover, except for DeepLines in the Hexafloat test-case, ultimate
432 loads always occur in DLC 6.2, where in addition to +/- 30° incoming wave heading, yaw misalignment is present.
433 For brevity reasons, we chose to focus mostly on fore-aft loads in this study, which are higher than in-plane/side-side loads, as
434 the incoming wind is always directed in the fore-aft direction in this study. However, as shown in further detail in (Papi et al.,
435 2023), in all three test-cases a strong correlation between platform roll and side-side tower base bending moment (TB Mx) is
436 present, indicating that these ultimate loads are hydrodynamics-driven. In fact, as the RNA and tower are heavy components,
437 gravitational and inertial loads can be significant on FOWT towers. Regarding specific test-cases, in OC4 TB Mx ultimate load
438 is approximately 16% lower in OpenFAST. This discrepancy is mainly caused by response at the tower natural frequency in
439 QBlade, which is not present in OpenFAST. On the other hand, if time series of TB Mx are compared for the Softwind test-case,
440 little variation can be noted between the three codes. For this load sensor the difference between QBlade and OpenFAST ultimate
441 loads that is shown in Fig. 5, is amplified by the maximum averaging technique. As described in Sect. 2.4, the ultimate load in
442 load cases with multiple turbulent seeds is computed as the maximum value closest to the mean of the maximums recorded
443 across all the turbulent seeds. Therefore, because ultimate loads are slightly different in QBlade and OpenFAST, the peak load
444 closest to the mean is recorded in different seeds for the two codes. This demonstrates how small differences between the models
445 can be amplified by the post-processing technique.

446 Maximum tower base fore-aft bending moment (TB My) is also recorded in parked conditions in the Softwind test-case - DLC
 447 6.2 for QBlade and OpenFAST and DLC 6.1 for DeepLines. Analyzing the times series of TB My in DLC 6.1 (Fig. 7) when
 448 peak load is recorded in DeepLines, the ultimate load is generated by a combination of gravitational and inertial loading resulting
 449 from platform motion. Higher values of platform pitch are noted in DeepLines, possibly a result of the slacker mooring lines in
 450 DeepLines, which explain the higher TB My. On the other hand, in the Hexafloat and OC4 test-cases, maximum TB My is found
 451 in DLC1.6 for all codes (Fig. 5). In both the latter cases OpenFAST and DeepLines are approximately 5% and 3% lower than
 452 QBlade in this metric. In this case ultimate loads are recorded around rated wind speed, similarly to BR Myc. Differently from
 453 the latter, which is analyzed in detail in Fig. 6, in the case of TB My, platform motion contributes directly to tower base loading
 454 as it increases gravitational and inertial forces. Overall, the three codes are close in this metric confirming that all three are able
 455 to capture the system dynamics in presence of extreme waves to a similar degree.



456

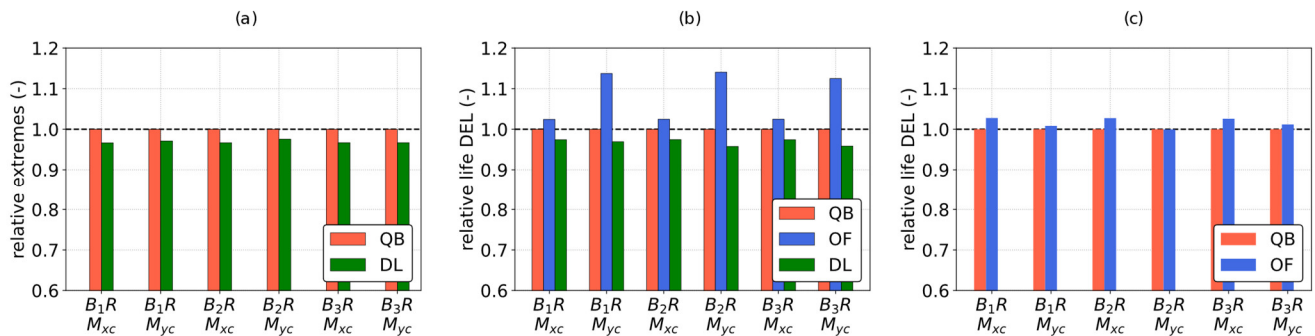
457 **Figure 7: Time series of fore-aft tower base bending moment of the Softwind model in DLC 6.1, ($w_s = 37$ m/s, $H_s = 16.5$), where**
 458 **maximum bending moment is recorded for OpenFAST. Tower base fore-aft bending moment (a), platform pitch (b), nacelle fore-aft**
 459 **acceleration (c), blade pitch (d), and wave height at platform reference position (e), rotor speed (f), aerodynamic thrust (not available**
 460 **in DeepLines outputs) (g), wind speed at hub height (h). DeepLines data are missing in (d,f,h) as these data cannot be exported from**
 461 **the code when the controller is not used.**

462

463 4.3 Fatigue Loads

464 4.3.1 Blade Root Fatigue Loads

465 Lifetime, zero-mean DELs computed with the procedure highlighted in Sect. 2.4 at blade root in the coned coordinate system
466 are shown in Fig. 8. Contrary to extreme loads, a clear trend is apparent in this case. In fact, with respect to QBlade, Lifetime
467 DELs are lower in DeepLines but higher in OpenFAST. In particular, 1Hz DELs are 3-5% lower than QBlade for DeepLines,
468 with little variation across the three blades. Indeed, fatigue loads are consistent among the three blades for all three codes and
469 all three test-cases, indicating good statistical convergence. Comparing QBlade and OpenFAST, blade root fatigue loads are
470 very close (0-3%) in case of the OC4 test-case, while increases of up to 12% in out-of-plane blade root bending moments can be
471 seen for Softwind. On the other hand, OpenFAST and QBlade are closer in the prediction of in-plane root bending moments
472 than out-of-plane root bending moments. The former are mainly driven by gravity, explaining the smaller differences between
473 the compared wind turbine simulation codes.



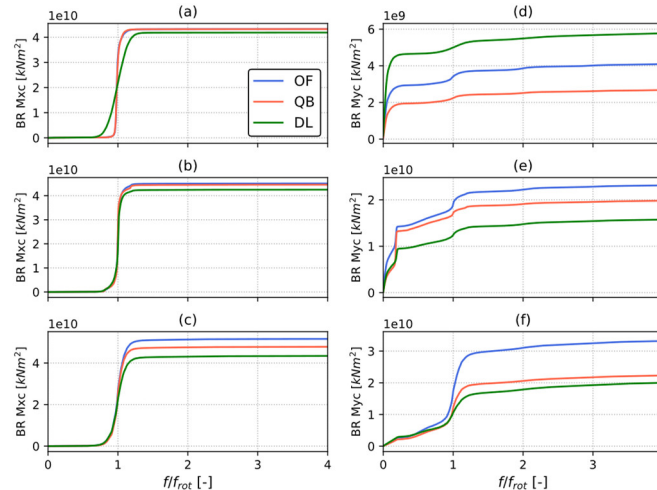
474

475 **Figure 8: Blade root fatigue loads in coned coordinate system: lifetime DELs normalized respect to values computed in QBlade. From**
476 **left to right: DTU 10MW Hexafloat, DTU 10MW Softwind and NREL 5MW OC4.**

477 To better understand the differences in Lifetime DELs, the Cumulative Power Spectral Density (CPSD) of blade root bending
478 moments for the Softwind FOWT design are shown in Fig. 9. They are obtained as the cumulative sum of the PSD of the signal.
479 A CPSD plot is read from left to right; steps in the data indicate peaks in the underlying PSD. When comparing two signals, the
480 increase or decrease in distance between the lines indicates the differences between them. The CPSDs for the Hexafloat FOWT
481 design look very similar and are not shown here for brevity as similar conclusions can be drawn. At all three of the examined
482 wind speeds (7 m/s, 13 m/s and 23 m/s) 1P loads are the main contributors to in-plane fatigue loading (BR M_{xc}). The magnitude
483 of 1P excitation is lower in DeepLines for all three wind speeds. The most relevant differences in this regard can be seen at 7
484 m/s (Fig. 9 (a)) and can be explained by the difference in rotor speed that was noted in Fig. 3. Because minimum rotor speed is
485 not imposed in DeepLines, while it is in QBlade and OpenFAST, the 1P peak spans a larger frequency range in the former and
486 is lower in magnitude.

487 Differences are also present in the BR M_{yc} CPSD. The near absence of response between 1P and 2P, at wave frequency, indicates
488 that apparent wind variations caused by platform motions do not induce relevant fatigue loading for this FOWT design. Three

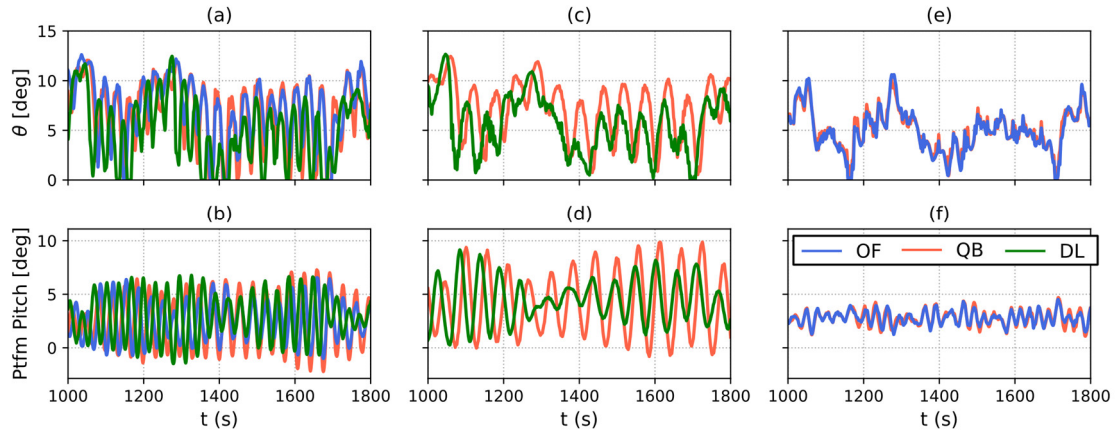
489 distinct phenomena drive the differences in this load sensor at the three wind speeds shown in Fig. 9. At 7 m/s (Fig. 9 (d)) wind
 490 speed OpenFAST and DeepLines show higher low-frequency excitation than QBlade. This phenomenon deserves further
 491 attention and will be discussed later in this Section when similar results for the OC4 FOWT design are presented. Moreover,
 492 while small in magnitude when compared to low-frequency response, the 1P peak is larger in OpenFAST. 1P BR Myc load
 493 variation remains larger for OpenFAST across the wind speed range, but are most noticeable at 23 m/s (Figs. 10 (f)).



494

495 **Figure 9: Cumulative Power Spectral Density (PSD) of blade root in-plane (a-c) and out-of-plane (d-f) bending moment for the**
 496 **Softwind test-case. Frequency is normalized by mean revolution frequency. PSD is computed on all simulations with 7 m/s (a, d), 13**
 497 **m/s (b, e) and 23 m/s (c, f) mean wind speed.**

498 Finally, at 13 m/s the three codes differ mainly in the low-frequency region, where the predicted response in OpenFAST is larger.
 499 Moreover, at this wind speed a large peak at the floater pitch natural frequency can also be seen, especially for QBlade. This
 500 peak in response at the floater natural frequency is caused by blade pitch – floater pitch self-excitation. As described in detail in
 501 (Larsen and Hanson, 2007), on a FOWT an increase in blade pitch causes aerodynamic loads to decrease, and the platform to
 502 swing forward as a consequence. In turn this causes the apparent wind speed on the rotor to increase and rotor speed to follow.
 503 The controller will thus react to the increased rotor speed by increasing blade pitch even further. A similar unstable behavior is
 504 triggered by a decrease in blade pitch, in this case the platform swings backward, reducing apparent wind speed and rotor speed,
 505 promoting further blade pitch reductions. As explained in Sect. 3.3, controller gains were reduced to avoid this phenomenon (see
 506 (Larsen and Hanson, 2007) for a detailed explanation on the effectiveness of this strategy). Despite this, as confirmed by the
 507 increased platform pitch standard deviation in Fig. 3 and blade pitch standard deviation in Fig. 4, unstable behavior emerged at
 508 11 and 13 m/s wind speed. This can be seen clearly in Fig. 10, where the time series of platform pitch and blade pitch for the
 509 three FOWT designs during a 13 m/s DLC 1.2 simulation are shown - and also in Fig 17 (d) later on in this study. In Fig. 10, the
 510 OC4 model is not affected by pitch self-excitation, while the Hexafloat and Softwind models are. In the latter two models,
 511 DeepLines is the least influenced by the phenomenon and QBlade is the most affected, despite all three codes using the same
 512 controller.



513

514 **Figure 10: Time series of blade pitch (top row) and platform pitch (bottom row) for a 13 m/s simulation in DLC 1.2. Softwind (a, b),**
 515 **Hexafloat (c, d) and OC4 (e, f).**

516

517

518

519

520

521

522

523

524

525

526

527

528

529

530

531

532

533

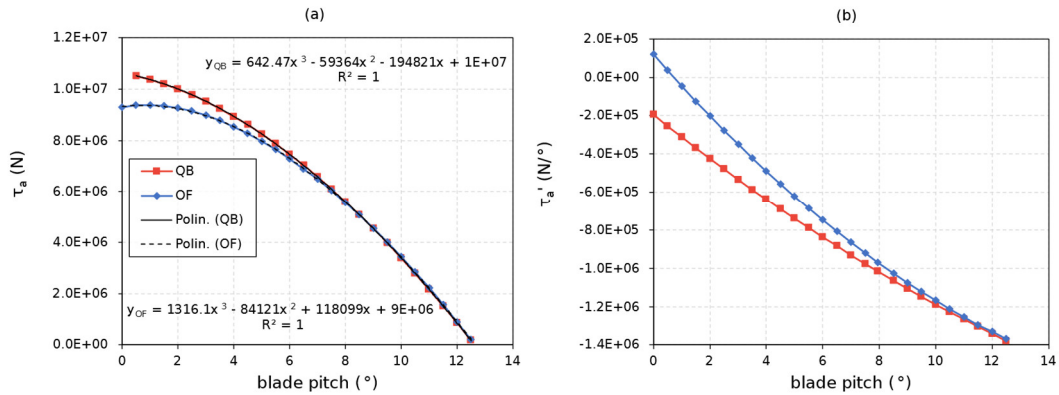
534

Various physical phenomena could cause such a difference in excitation. However, by process of exclusion, differences in hydrodynamic excitation are unlikely to be the cause of the increased self-excitation in QBlade, as nearly identical response in QBlade and OpenFAST was noted at the Softwind’s pitch natural frequency in part one of this study ((Behrens De Luna et al., 2023), Fig. 13). Moreover, the way unsteady aerodynamics are modelled is also not the cause, as switching to DBEM in QBlade did not improve agreement in this regard with respect to OpenFAST (not shown herein for brevity). In addition, as stated previously, OpenFAST does not include blade torsion. However, switching to a rigid structure did not improve the agreement of OpenFAST and QBlade. A possible explanation for the difference in blade pitch - platform pitch self-excitation was put forward in part one of this study (Behrens De Luna et al., 2023) and is related to increased aerodynamic torque variation in QBlade with respect to the other two codes. Indeed, upon further investigations, differences in the system dynamics, and how they interact with the control system, could explain the observed behavior. As explained in detail by Abbas et al., (2022), the controller and turbine can be seen as a closed-loop second-order system, characterized by a natural frequency at a certain operating wind speed:

$$\omega^2 = k_i(U_{op})B = k_i(U_{op}) \frac{N_g \partial \tau_a}{J \partial \beta} \quad (1)$$

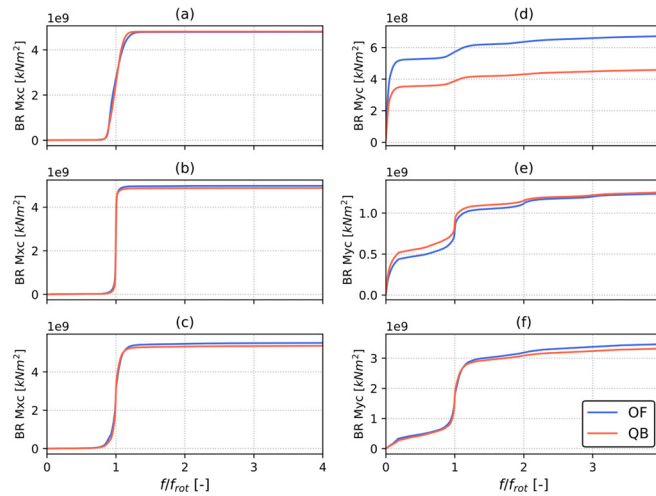
where N_g and J are the gearbox ratio and rotor inertia, which are the same in OpenFAST, QBlade and DeepLines. The higher the natural frequency, the more responsive the system is to an external disturbance such as a platform pitch oscillation. The integral controller gain k_i is also the same in the two codes, as it depends on the controller tuning. The slope of the aerodynamic torque as a function of blade pitch is, however, different in the two codes. The derivative of aerodynamic torque as a function of blade pitch for the mean 11 m/s operating conditions is shown in Fig. 11 (b). As $\frac{\partial \tau_a}{\partial \beta}$ is larger in magnitude for QBlade at the mean operating blade pitch of approximately 0.5° , from eq. 1, ω^2 is also larger, leading to increased self-excitation in

535 QBlade. This highlights how small differences in aerodynamics can lead to different controller response and influence turbine
 536 load predictions significantly.



537
 538 **Figure 11: (a) aerodynamic torque as a function of blade pitch for OpenFAST and QBlade for 11 m/s operating TSR,**
 539 **and relative trendlines. (b) derivative of aerodynamic torque as a function of blade pitch computed from analytic**
 540 **derivative of trendlines.**

541 Despite QBlade and OpenFAST lifetime DELs being very close, the OC4 FOWT design highlights some interesting behavior,
 542 and differs in some key aspects from the Softwind FOWT design. CPSDs of blade root bending moments can, again, help
 543 investigate the causes of the differences in Lifetime DELs and are shown in Figure 12. Focusing on out-of-plane root bending
 544 moment (TB My), differences in 1P excitation that are highlighted for the Softwind design (Fig. 9) are not apparent in OC4. The
 545 larger difference in 1P excitation between models on the Softwind design with respect to the OC4 design can likely be explained
 546 by the size difference of the two rotors. As found by Madsen et al., (2020) non-uniform rotor loading due to turbulence and wind
 547 shear increases with rotor size. For a larger rotor, a higher portion of the turbulent flow structures feature a length scale that is
 548 smaller than the rotor diameter, shifting a higher ratio of the total energy in the turbulent spectrum from lower frequencies to the
 549 1P frequency and multiples. As for wind shear, a larger rotor operates in a larger portion of the atmospheric boundary layer,
 550 meaning that each blade experiences more inflow variation during a revolution. As these phenomena increase in magnitude they
 551 are expected to increase the differences between aerodynamic models at 1P frequency.

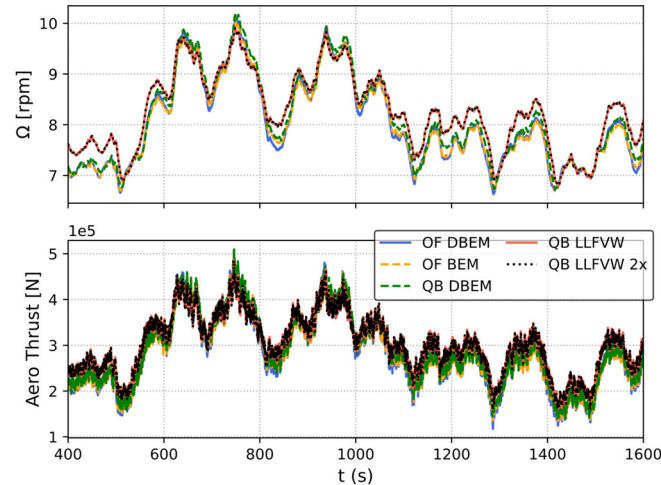


552

553

554

Figure 12: Cumulative Power Spectral Density (CPSD) of blade root in-plane (a-c) and out-of-plane (d-f) bending moment for the OC4 model. PSD is computed on all simulations with 7 m/s (a, d), 13 m/s (b, e) and 23 m/s (c, f) mean wind speed.



555

556

557

558

Figure 13: Time series of rotor speed and aerodynamic thrust in a 7 m/s simulation of the OC4 test-case. Various wake models are compared; OpenFAST DBEM (Branlard et al., 2022), OpenFAST BEM (Ning et al., 2015), QBlade DBEM (Madsen et al., 2020) and QBlade LLFVW (Marten, 2020).

559

560

561

562

563

564

565

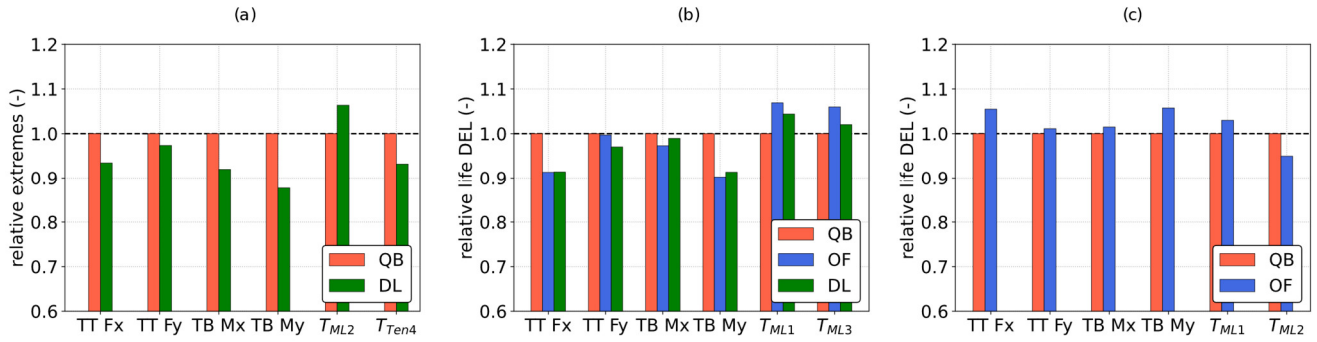
On the other hand, the low frequency excitation difference that was noted for the Softwind design is also found for the OC4 design (Fig. 12 (d)) and, although not shown herein for brevity, is also found to be one of the main drivers of the higher Lifetime DELs in OpenFAST (Fig. 8). To better understand this difference, additional simulations were carried out with additional aerodynamic models in both QBlade and OpenFAST in an attempt to isolate the cause of such differences. In particular, OpenFAST simulations were performed using quasi-steady BEM without dynamic induction corrections (OpenFAST BEM). QBlade on the other hand was run using LLFVW with doubled wake length (LLFVW x2) and with the polar-BEM method (Madsen et al., 2020) (QBlade DBEM). Time series of rotor speed and aerodynamic thrust are shown in Fig. 13 for a 7 m/s mean

566 wind speed simulation in DLC 1.2. As shown in Fig. 13, larger variations in rotor speed can be noted in the BEM-based models.
567 This phenomenon is present in both QBlade and OpenFAST and no improvement with respect to QBlade LLFVW is noted when
568 a dynamic induction correction is used. On the other hand, doubling the wake length in the LLFVW simulation has little to no
569 effect on rotor speed, indicating that the wake cut-off length used in the study is adequate. The larger rotor speed variation in
570 BEM models causes rotor thrust to vary more as TSR varies, thus causing the additional low-frequency loading shown in Fig.
571 13.

572 These results can be put into perspective by comparing them to other authors' findings. Indeed, differences between BEM-based
573 and LLFVW aerodynamic models in the prediction of blade root fatigue loads have also been noted by other authors. Boorsma
574 et al. (2020) attributed the differences observed at 1P frequency to different induction tracking of the BEM models during blade
575 revolution, which causes differences in aerodynamic loading amplitude if wind shear, yaw misalignment, rotor tilt and, in the
576 case of FOWTs, platform pitch are present. In addition to 1P differences, Perez-Becker et al. (2020) also noted differences
577 between LLFVW and BEM at low frequencies, the latter mainly being caused by different blade pitch actuation in the models.
578 In the context of FOWTs, Corniglion (2022) also found blade root fatigue loads predicted with a LLFVW model to be lower
579 than those computed with a BEM-based aerodynamic tool. In this context, the higher fatigue loads that are noted in OpenFAST
580 are in line with these findings. However, the same cannot be said for DeepLines that predicts lower lifetime DELs than the
581 LLFVW-based QBlade.

582 **4.3.1 Tower Base and Mooring Fatigue Loads**

583 Tower top, tower base and mooring lifetime DELs are shown in Fig. 14 for the three FOWT designs. The OC4 and Hexafloat
584 designs show a similar trend to those shown in Fig. 8; lower lifetime DELs for DeepLines and higher Lifetime DELs for
585 OpenFAST. However, the differences in fore-aft tower lifetime DELs (TT F_x, TB M_y) in Fig. 14 (a) and (c) are larger than those
586 in out-of-plane blade root lifetime DELs in Fig. 8 (a) and (c). Such phenomenon can be traced back, at least in part, to the
587 differences in platform pitch that are noted in Fig. 4, which cause larger or smaller variations in gravitational and inertial forces
588 on the tower, increasing the difference in tower lifetime DELs. Differently from blade root fatigue loads however, OpenFAST
589 and DeepLines show good agreement in terms of lifetime DELs in Fig. 14 for the Softwind design. Tower-related fatigue loads
590 are lower than QBlade, while mooring line fatigue predictions are higher. Moreover, differences in side-side tower loads (TT F_y
591 and TB M_x) appear to be smaller than those found in the respective fore-aft sensors (TT F_x and TB M_y). These load sensors are
592 arguably less influenced by aerodynamics, as the wind is always aligned with the global X direction, and more influenced by
593 hydrodynamics, as wave headings range from -150° to 150°. In this context the good agreement in side-side loads is expected
594 as hydrodynamics are modeled similarly in all three codes.



595

596

597

598

Figure 14: Lifetime DELs normalized with respect to values computed in QBlade. Yaw bearing shear forces in p coordinate system and tower base fore-aft and side-side bending moments and shear forces in t coordinate system. From left to right: DTU 10MW Hexafloat, DTU 10MW Softwind and NREL 5MW OC4.

599

The differences between the three models can be analyzed in more detail by comparing 1Hz DELs weighted by the probability of each environmental condition to occur:

600

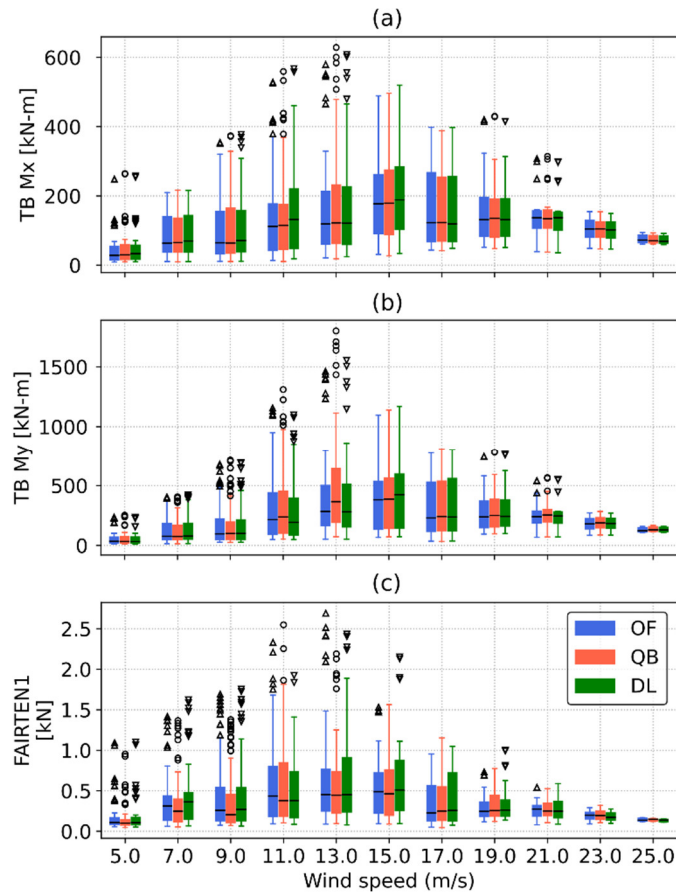
601

$$\overline{DEL}_i = p_i * DEL = p_i \left(\frac{\sum_j n_j A_j^m}{t} \right)^{1/m} \quad (2)$$

602

p_i is the probability of each condition to occur, n_j and A_j are the combinations of rainflow counted j-th number of cycles and amplitude in each simulation and m is the Wöhler curve exponent, equal to 10 for the composite blades and 4 for the other steel components. As discussed in Sect. 2.4, 1Hz DELs multiplied by their respective probability of occurrence are representative of the contribution to lifetime fatigue loads of each operating condition.

605

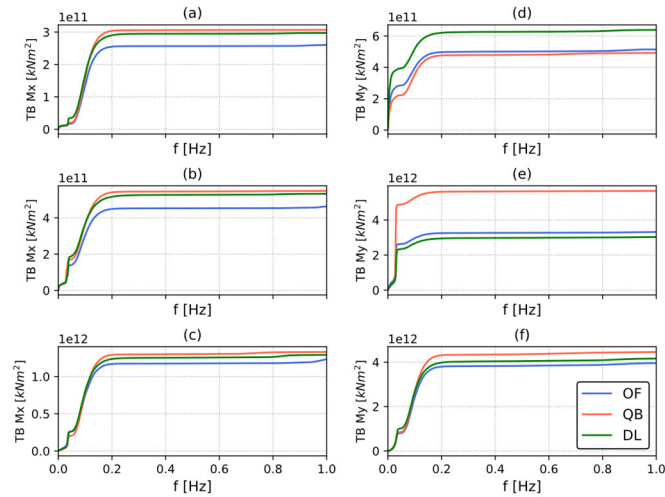


606

607 **Figure 15: Statistics of tower base bending moment and fairlead tension 1Hz zero-mean Damage Equivalent Loads weighted by the**
 608 **probability of each environmental bin they refer to for the Softwind model. The boxes represent the 1st and 3rd quartiles, the whiskers**
 609 **represent the data range and are found by adding/subtracting to the box edges 1.5 times the interquartile (IQR) range, the horizontal**
 610 **line is the median of the data and outlier values are shown as scatter points.**

611

612 Statistics of tower base and fairlead tension of one of the upwind mooring lines 1Hz DELs for the Softwind design are shown in
 613 Fig. 15. From a fatigue damage standpoint, the most relevant wind speeds are included between 9 m/s and 19 m/s wind speed.
 614 While 1Hz DELs are very close for all three numerical codes in Fig. 15 (a), the analysis of Fig. 15 (b) can help pinpoint the root
 615 cause of the increased Lifetime DEL prediction in QBlade. In fact, while the three codes agree well across most wind speeds,
 616 1Hz DELs are statistically higher for QBlade particularly in the 11 m/s and 13 m/s wind speed bins. The CPSDs of tower base
 617 bending moments for the 7 m/s, 13 m/s and 23 m/s wind speed bins are shown in Figure 16. It stands out that tower base excitation
 618 is dominated by low-frequency peaks, corresponding to the floater's natural surge/sway and pitch/roll natural frequencies, and
 619 by response in the wave excitation frequency band. Moreover, contrary to blade root loads, 1P and 3P excitation is nearly
 irrelevant as the CPSDs show a flat profile from 0.2 Hz and upwards.



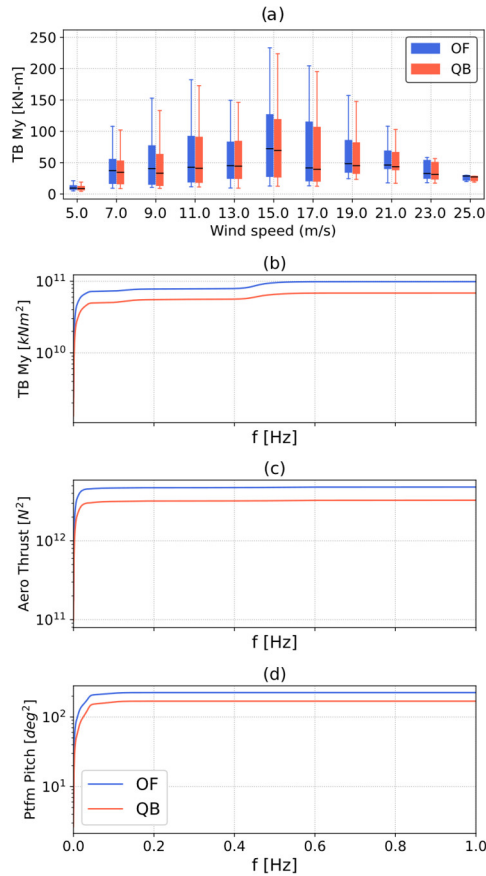
620

621 **Figure 16: Cumulative Power Spectral Density (CPSD) of tower base side-side (a-c) and fore-aft (d-f) bending moment for the Softwind**
 622 **test-case. CPSD is computed on all simulations with 7 m/s (a, d), 13 m/s (b, e) and 23 m/s (c, f) mean wind speed.**

623 Regarding fore-aft bending moment (TB My), at 7 m/s (Fig. 16 (d)), low-frequency aerodynamic excitation is the main driver
 624 of differences between QBlade – that shows lower response and fatigue loads at this wind speed – and the BEM-based codes.
 625 These differences are caused by the higher rotor speed variations recorded in OpenFAST and especially in DeepLines, as
 626 minimum rotor speed is not enforced in this code. The higher rotor speed variation leads to higher variation in aerodynamic
 627 forcing, as shown in Fig. 13. This phenomenon also contributes to the higher platform pitch variation that is observed for the
 628 BEM based codes (Fig. 4), further increasing low-frequency TB My excitation.

629 When analyzing Fig 16 (e), higher response at the floater pitch natural frequency is noted in QBlade. The cause of the increased
 630 response is floater-pitch blade-pitch instability, discussed in detail in Sect. 4.3.1

631 The same phenomenon also impacts the OC4 testcase, as shown in Fig. 17. The largest differences between OpenFAST and
 632 QBlade in the fore-aft tower base bending moment 1Hz DELs are located in the 9 m/s wind speed bin (Fig. 17 (a)). The CPSDs
 633 of aerodynamic thrust, platform pitch and TB My (Figs. 17 (b,c,d)) show that the main differences between the codes are found
 634 at very low frequencies, and are again caused by differences in aerodynamic response that are amplified by platform pitch and
 635 rotor speed variations.



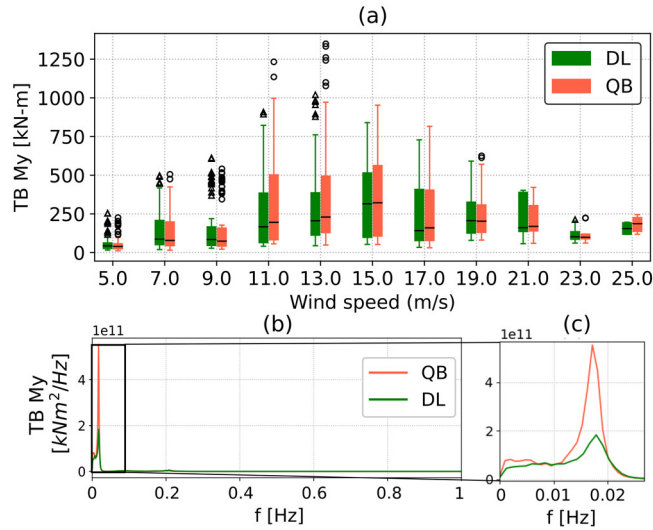
636

637 **Figure 17: (a) Statistics of tower base fore-aft bending moment 1Hz zero-mean Damage Equivalent Loads weighted by the probability**
 638 **of each environmental bin they refer to for the OC4 model. The boxes represent the 1st and 3rd quartiles, the whiskers represent the**
 639 **data range and are found by adding/subtracting to the box edges 1.5 times the interquartile (IQR) range, the horizontal line is the**
 640 **median of the data and flier values are shown as scatter points. (b,c,d) Cumulative Power Spectral Density (CPSD) of tower base fore-**
 641 **aft bending moment, aerodynamic thrust and platform pitch for the OC4 design. PSD is computed on all simulations with 9 m/s mean**
 642 **wind speed.**

643 Going back to the Softwind FOWT concept, at 13 m/s (Fig. 16 (e)) the largest difference between QBlade and the other codes
 644 is at the floater pitch natural frequency, where TB My PSD is much larger in the former code. The higher response is caused by
 645 the same phenomenon that causes higher blade root CPSDs at 13 m/s wind speed in QBlade (Fig. 9): floater and blade pitch self-
 646 excitation. In the case of tower base loads, in addition to cyclic variation in aerodynamic loads, cyclic inertial and gravitational
 647 forcing become relevant load sources, as the weight of the tower itself and the Rotor Nacelle Assembly (RNA) are considerable.
 648 Therefore, despite QBlade comparing well to the other two codes at other wind speeds (Fig. 16 (f)), the difference highlighted
 649 at 13 m/s (Fig. 16 (e)) ultimately leads to higher TB My lifetime DELs for QBlade (Fig. 14).

650 As shown in Fig. 18, floater and blade pitch self-excitation also influence fatigue load predictions for the Hexafloat model. As
 651 discussed previously, DeepLines predicts lower lifetime DELs than QBlade for this test-case. Contrary to floater-pitch-frequency

652 excitation, the peak in TB My response in correspondence of the tower first fore-aft natural frequency located at 0.2 Hz is
 653 captured well by both DeepLines and QBlade (Fig. 18 (b,c)).



654
 655 **Figure 18: (a) Statistics of fore-aft tower base bending moment 1Hz zero-mean Damage Equivalent Loads weighted by the probability**
 656 **of each environmental bin they refer to for the Hexafloat model. The boxes represent the 1st and 3rd quartiles, the whiskers represent**
 657 **the data range and are found by adding/subtracting to the box edges 1.5 times the interquartile (IQR) range, the horizontal line is the**
 658 **median of the data and outlier values are shown as scatter points. (b) Power Spectral Density (PSD) of tower base fore-aft bending**
 659 **moment for the Hexafloat test-case. PSD is computed on all simulations with 11 m/s mean wind speed.**

660 5 Conclusions

661 An extensive code-to-code comparison with realistic environmental conditions is performed in this study. Three floating wind
 662 turbine substructure designs, a semi-submersible, a spar-buoy and the Hexafloat concept proposed by Saipem are compared in
 663 multiple environmental conditions involving hundreds of simulations. The considered codes include TU Berlin's QBlade,
 664 NREL's OpenFAST and Principia's DeepLines. Statistics, extreme and fatigue loads of key load sensors are discussed.
 665 OpenFAST and QBlade results were refined over the span of several months, correcting small bugs that may arise in such a
 666 complex set-up and ultimately aligning the models better. DeepLines has not benefitted from such improvements due to budget
 667 and time limitations, which explains the poorer agreement noted for this code in many instances. These results are nevertheless
 668 included as they are representative of what could be achieved with limited time and budget often connected to industrial
 669 processes.

670 The statistical comparison revealed good agreement between the codes in their ability to predict general system dynamics.
 671 Nonetheless some differences, particularly in the coupling with the controller, emerged. Blade pitch – floater pitch self-excitation
 672 is noted in the Softwind and Hexafloat designs. While this phenomenon is present in all three codes, it is more accentuated in
 673 QBlade, despite all three sharing the blade pitch controller logic. A possible explanation for this phenomenon was put forward
 674 by the authors in the first part of this study (Behrens De Luna et al., 2023) and is linked to larger variations in rotor speed in

675 QBlade. Above rated wind speed, such variations cause the pitch controller to intervene more aggressively, thus triggering the
676 floater pitch instability. Upon further investigation, aerodynamic torque is found to be more sensitive to blade pitch variations
677 at low wind speeds in QBlade, which causes the response of the coupled turbine and controller system to be faster and thus more
678 prone to instability. This self-excitation is found to be the cause of increased fore-aft tower base and out-of-plane root bending
679 moment lifetime DELs in QBlade in both the Hexafloat and Softwind designs and demonstrated how small differences in
680 modeling can have a significant impact on design loads.

681 No clear trend is noted when ultimate loads are compared. Taking QBlade as a reference point, ultimate loads are regularly found
682 to be in the $\pm 15\%$ range, with only some exceeding it. Although not discussed in detail in this work, part of these differences
683 stem from the fact that the compared ultimate loads are selected according to the so-called “*mean of max*” method according to
684 international standard indications (IEC61400-1, Annex G). As shown in (Papi et al., 2023), small differences in ultimate loads
685 may cause the method to select a different maximum, amplifying the difference between the models. In addition, the different
686 FOWT designs have a different dynamical response to the environmental conditions, thus affecting the ultimate loads differently.
687 Fatigue loads, namely lifetime DELs, show a clear trend: OpenFAST generally predicts higher loads than QBlade, while
688 DeepLines predicts lower lifetime fatigue loads. The reason for the latter being a different model set-up of the Softwind design
689 in DeepLines and the lower effect of the blade pitch-platform pitch instability in the Hexafloat design. The exception to this is
690 represented by tower base lifetime DELs, which for the Softwind design, are lower in OpenFAST. The root cause of this behavior
691 in the Softwind design is again the floater pitch – blade pitch interaction, which is higher in QBlade compared to the two other
692 codes. The higher DELs in OpenFAST are in line with other authors’ findings, who observed higher fatigue loads in BEM-based
693 codes compared to in LLFVW-based codes. In this study however, OpenFAST differs from the other two codes also in the
694 structural modeling: the former utilizing a modal structural model without the ability to model blade torsion while the latter two
695 feature a multi-body model that includes blade torsion. Despite the trend being consistent between the codes, the magnitude of
696 the lifetime DEL overestimation is different in the two designs where OpenFAST and QBlade are compared, OC4 and Softwind.
697 In fact, in Softwind, blade root DELs are 2% to 14% higher in OpenFAST, while in OC4 they are up to 1.5% higher. The
698 analysis of CPSDs highlighted greater response at the 1P frequency in OpenFAST in the former design, while in OC4 the main
699 difference between OpenFAST and QBlade is mostly confined to higher response in OpenFAST at very low frequencies. This
700 low frequency difference is driven by increased rotor speed variation, in turn caused by differences in aerodynamic modeling.
701 In conclusion, the relatively simpler model assumptions adopted in OpenFAST are found to be able to reproduce the system
702 dynamics adequately for the considered designs. No clear trend is noted for extreme loads. In fact, these differences could not
703 be traced back to a specific engineering model or modelling choice. In this regard, including a larger set of extreme load cases
704 with more parameter variations could help give a clearer picture of the differences in ultimate loading between the codes and the
705 FOWT designs. On the other hand, a clear trend is noted in fatigue loads. This may be explained by the difference in aerodynamic
706 models, in particular the comparison between the BEM-based OpenFAST and the LLFVW-based QBlade is consistent with
707 existing scientific literature. DeepLines however contradicts this trend. While this may be, at least in part, due to setup differences

708 in the Softwind design and to this code being less prone to blade pitch-floater pitch self-excitation, this aspect is identified as a
709 key point for future research.

710 Overall, the main outcomes of this study can be summarized as follows: i) the differences between the compared modelling
711 theories are consistent with the existing body of literature on onshore wind turbines. ii) the greater movement that FOWTs are
712 allowed did not exacerbate the differences to the point that simpler models, such as OpenFAST, are outdated. These tools remain
713 reliable for extreme load estimation. For fatigue loads, underestimation with respect to more physically accurate theories of 2-
714 15% depending on the specific load sensor can be expected. Therefore, within the limitations highlighted in this and other similar
715 works, these models are still relevant for industry and for many research applications.

716

717 **Nomenclature**

718	COD	Co-Directional
719	CPSD	Cumulative Power Spectral Density
720	CS	Coordinate System
721	DLC	Design Load Case
722	$E[\varepsilon_1 \varepsilon_2]$	Expected value of ε_1 conditioned on ε_2
723	ECD	Extreme Change of Direction with coherent gust
724	ESS	Extreme Sea State
725	ETM	Extreme Turbulence Model
726	EWM	Extreme Wind Model
727	FOWT	Floating Offshore Wind Turbine
728	MUL	Multi-Directional
729	NSS	Normal Sea State
730	NTM	Normal Turbulence Model
731	OC4	OC4 DeepCWind semi-submersible
732	PSD	Power Spectral Density
733	Sims.	Simulations
734	SSS	Severe Sea State
735	H_s	Significant Wave Height (m)
736	T_p	Peak Spectral Period (s)
737	M_{WW}	Mean Wind-Wave misalignment ($^\circ$)
738	U_w	Wind Speed
739	V_{in}/V_{out}	Cut-in/Cut-out wind speed (m/s)
740	ws	Wind speed

741



Funding This work has received support from the FLOATECH project, funded by the European Union’s Horizon 2020 research and innovation programme under grant agreement No. 101007142

744

745 **Data Availability** The simulation results used in this study are publicly available at 10.5281/zenodo.7254241. The met-ocean
746 conditions are also available at doi.org/10.1088/1742-6596/2385/1/012117. The QBlade-Ocean models upon which the models
747 tested herein are based are available at 10.5281/zenodo.6397352 (OC5), 10.5281/zenodo.6397358 (Softwind),
748 10.5281/zenodo.6397313 (Hexafloat) and the modifications required to align them with the models tested herein are detailed in
749 10.5281/zenodo.7817707.

750

751 **Competing Interest** At least one of the (co-)authors is a member of the editorial board of Wind Energy Science. The peer-
752 review process was guided by an independent editor, and the authors also have no other competing interests to declare.

753 **References**

754 Abbas, N. J., Zalkind, D. S., Pao, L., and Wright, A.: A reference open-source controller for fixed and floating offshore wind
755 turbines, *Wind Energy Science*, 7, 53–73, <https://doi.org/10.5194/wes-7-53-2022>, 2022.

756 Antonia Krieger, Gireesh K. V. Ramachandran, Luca Vita, Pablo Gómez Alonso, Gonzalo Gónzales Almeria, Joannès Barque,
757 and Goren Aguirre: D7.2 LIFEs50+ Design Basis, 2015.

758 Arnal, V.: Experimental modelling of a floating wind turbine using a “software-in-the-loop” approach, These de doctorat,
759 Ecole centrale de Nantes, 2020.

760 Bak, C., Zahle, F., Bitsche, R., Taeseong, K., Anders, Y., Henriksen, L. C., Natarajan, A., and Hansen, M. H.: Description of
761 the DTU 10MW Reference Wind Turbine, DTU Wind Energy, Roskilde, Denmark, 2013.

762 Behrens De Luna, R., Perez-Becker, S., Saverin, J., Marten, D., Papi, F., Ducasse, M.-L., Bonnefoy, F., Bianchini, A., Nayeri,
763 C. N., and Paschereit, C. O.: Verifying QBlade-Ocean: A Hydrodynamic Extension to the Wind Turbine Simulation Tool
764 QBlade, *Wind Energy Science Discussions*, 1–36, <https://doi.org/10.5194/wes-2023-117>, 2023.

765 Bergua, R. and et. al.: OC6 Project Phase III: Validation of the Aerodynamic Loading on a Wind Turbine Rotor Undergoing
766 Large Motion Caused by a Floating Support Structure, *Wind Energy Science Journal*, 8, 465–485, <https://doi.org/10.5194/wes-8-465-2023>, 2023.

768 Boorsma, K., Wenz, F., Lindenbun, K., Aman, M., and Kloosterman, M.: Validation and accommodation of vortex wake
769 codes for wind turbine design load calculations, *Wind Energ. Sci.*, 5, 699–719, <https://doi.org/10.5194/wes-5-699-2020>, 2020.

770 Borg, M.: LIFES50+ Deliverable D1.2: Wind turbine models for the design, DTU Wind Energy, Risø, Denmark, 2015.

771 Branlard, E., Jonkman, B., Pirrung, G. R., Dixon, K., and Jonkman, J.: Dynamic inflow and unsteady aerodynamics models
772 for modal and stability analyses in OpenFAST, *J. Phys.: Conf. Ser.*, 2265, 032044, <https://doi.org/10.1088/1742-6596/2265/3/032044>, 2022.

774 Buhl, M.: MExtremes User’s Guide, 9, 2015.

775 Burton, T. (Ed.): *Wind energy: handbook*, J. Wiley, Chichester ; New York, 617 pp., 2001.

- 776 Corniglion, R.: aero-elastic modeling of floating wind turbines with vortex methods, PhD Thesis, École des Ponts ParisTech,
777 2022.
- 778 DNVGL: DNVGL-ST-0437 - Loads and site conditions for wind tubines, DNVGL AS, 2016.
- 779 DNVGL: DNVGL-ST-0119 - Floating wind turbine structures, DNVGL AS, 2018.
- 780 Faltinsen, O.: Sea Loads on Ships and Offshore Structures, Cambridge University Press, 1993.
- 781 Hansen, M. O. L.: Aerodynamics of wind turbines, 2nd ed., Earthscan, London ; Sterling, VA, 181 pp., 2008.
- 782 Haselsteiner, A. F., Lehmkuhl, J., Pape, T., Windmeier, K.-L., and Thoben, K.-D.: ViroCon: A software to compute
783 multivariate extremes using the environmental contour method, SoftwareX, 9, 95–101,
784 <https://doi.org/10.1016/j.softx.2019.01.003>, 2019.
- 785 Haselsteiner, A. F., Sander, A., Ohlendorf, J.-H., and Thoben, K.-D.: Global Hierarchical Models for Wind and Wave
786 Contours: Physical Interpretations of the Dependence Functions, in: Volume 2A: Structures, Safety, and Reliability, ASME
787 2020 39th International Conference on Ocean, Offshore and Arctic Engineering, Virtual, Online, V02AT02A047,
788 <https://doi.org/10.1115/OMAE2020-18668>, 2020.
- 789 Haselsteiner, A. F., Coe, R. G., Manuel, L., Chai, W., Leira, B., Clarindo, G., Guedes Soares, C., Hannesdóttir, Á., Dimitrov,
790 N., Sander, A., Ohlendorf, J.-H., Thoben, K.-D., Hauteclouque, G. de, Mackay, E., Jonathan, P., Qiao, C., Myers, A., Rode,
791 A., Hildebrandt, A., Schmidt, B., Vanem, E., and Huseby, A. B.: A benchmarking exercise for environmental contours, Ocean
792 Engineering, 236, 109504, <https://doi.org/10.1016/j.oceaneng.2021.109504>, 2021.
- 793 Hayman, G. J.: MLife Theory Manual for Version 1.00, NREL, 2012.
- 794 International Electrotechnical Commission: TS 61400-3-1, Wind energy generation systems - Part 3-1: Design requirements
795 for fixed offshore wind turbines, 2019a.
- 796 International Electrotechnical Commission: TS 61400-3-2, Wind energy generation systems - Part 3-2: Design requirements
797 for floating offshore wind turbines, 2019b.
- 798 Jonkman, B. J.: TurbSim User’s Guide v2.00.00, Renewable Energy, 2014.
- 799 Jonkman, J.: Definition of the Floating System for Phase IV of OC3, <https://doi.org/10.2172/979456>, 2010.
- 800 Jonkman, J. and Musial, W.: Offshore Code Comparison Collaboration (OC3) for IEA Task 23 Offshore Wind Technology
801 and Deployment, Renewable Energy, 74, 2010.
- 802 Jonkman, J., Butterfield, S., Musial, W., and Scott, G.: Definition of a 5-MW Reference Wind Turbine for Offshore System
803 Development, <https://doi.org/10.2172/947422>, 2009.
- 804 Jonkman, J. M. and Matha, D.: Dynamics of offshore floating wind turbines-analysis of three concepts, Wind Energ., 14, 557–
805 569, <https://doi.org/10.1002/we.442>, 2011.
- 806 Kurnia, R., Ducrozet, G., and Gilloteaux, J.-C.: Second Order Difference- and Sum-Frequency Wave Loads in the Open-
807 Source Potential Flow Solver NEMOH, ASME 2022 41st International Conference on Ocean, Offshore and Arctic
808 Engineering, <https://doi.org/10.1115/OMAE2022-79163>, 2022.

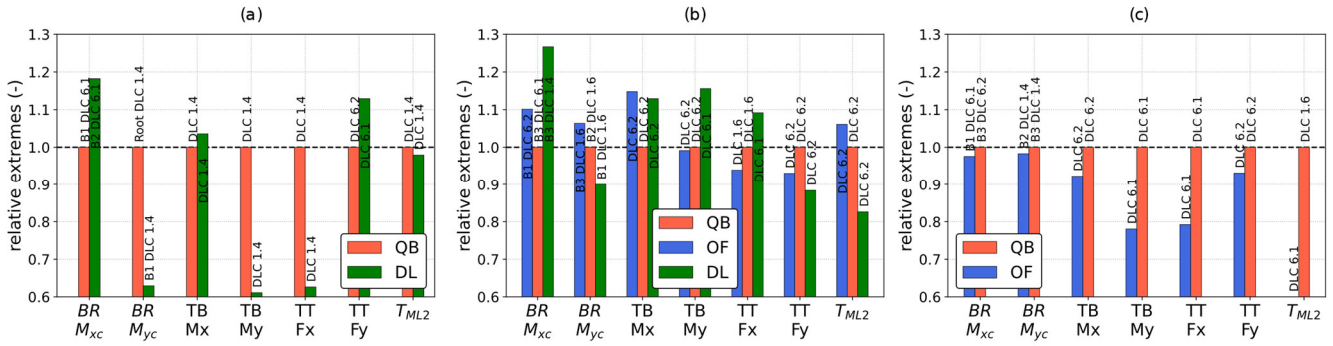
- 809 Larsen, T. J. and Hanson, T. D.: A method to avoid negative damped low frequent tower vibrations for a floating, pitch
810 controlled wind turbine, *J. Phys.: Conf. Ser.*, 75, 012073, <https://doi.org/10.1088/1742-6596/75/1/012073>, 2007.
- 811 Le Cunff, C., Heurtier, J.-M., Piriou, L., Berhault, C., Perdrizet, T., Teixeira, D., Ferrer, G., and Gilloteaux, J.-C.: Fully
812 Coupled Floating Wind Turbine Simulator Based on Nonlinear Finite Element Method: Part I — Methodology, in: Volume 8:
813 Ocean Renewable Energy, ASME 2013 32nd International Conference on Ocean, Offshore and Arctic Engineering, Nantes,
814 France, V008T09A050, <https://doi.org/10.1115/OMAE2013-10780>, 2013.
- 815 Lenfest, E., Goupee, A. J., Wright, A., and Abbas, N.: Tuning of Nacelle Feedback Gains for Floating Wind Turbine
816 Controllers Using a Two-DOF Model, in: Volume 9: Ocean Renewable Energy, ASME 2020 39th International Conference
817 on Ocean, Offshore and Arctic Engineering, Virtual, Online, V009T09A063, <https://doi.org/10.1115/OMAE2020-18770>,
818 2020.
- 819 Li, L., Gao, Z., and Moan, T.: Joint Distribution of Environmental Condition at Five European Offshore Sites for Design of
820 Combined Wind and Wave Energy Devices, *Journal of Offshore Mechanics and Arctic Engineering*, 137, 031901,
821 <https://doi.org/10.1115/1.4029842>, 2015.
- 822 Madsen, H. A., Larsen, T. J., Pirrung, G. R., Li, A., and Zahle, F.: Implementation of the blade element momentum model on
823 a polar grid and its aeroelastic load impact, *Wind Energy Science*, 5, 1–27, <https://doi.org/10.5194/wes-5-1-2020>, 2020.
- 824 Marten, D.: QBlade: a modern tool for the aeroelastic simulation of wind turbines, 2020.
- 825 Marten, D., Lennie, M., Pechlivanoglou, G., Nayeri, C. N., and Paschereit, C. O.: Implementation, optimization and validation
826 of a nonlinear lifting line free vortex wake module within the wind turbine simulation code qblade, *Proceedings of the ASME*
827 *Turbo Expo*, <https://doi.org/10.1115/GT2015-43265>, 2015.
- 828 Ning, A., Hayman, G., Damiani, R., and Jonkman, J. M.: Development and Validation of a New Blade Element Momentum
829 Skewed-Wake Model within AeroDyn, in: 33rd Wind Energy Symposium, 33rd Wind Energy Symposium, Kissimmee,
830 Florida, <https://doi.org/10.2514/6.2015-0215>, 2015.
- 831 Papi, F. and Bianchini, A.: Technical challenges in floating offshore wind turbine upscaling: A critical analysis based on the
832 NREL 5 MW and IEA 15 MW Reference Turbines, *Renewable and Sustainable Energy Reviews*, 162, 112489,
833 <https://doi.org/10.1016/j.rser.2022.112489>, 2022.
- 834 Papi, F. and Bianchini, A.: Annotated Guidelines for the Simulation of Floating Offshore Wind Turbines in a Real
835 Environment, in: *Proceedings of OMAE 2023, OMAE 2023, Melbourne, Australia, 2023*.
- 836 Papi, F., Behrens De Luna, R., Saverin, J., Marten, D., Combreau, C., Troise, G., Mirra, G., and Bianchini, A.: D2.3. Design
837 Load Case Database for Code-to-Code Comparison, 2022a.
- 838 Papi, F., Bianchini, A., Troise, G., Mirra, G., Marten, D., Saverin, J., Behrens De Luna, R., Ducasse, M.-L., and Honnet, J.:
839 D2.4. Full report on the estimated reduction of uncertainty in comparison to the state-of-the-art codes OpenFAST and
840 DeepLines Wind™, FLOATECH, 2022b.
- 841 Papi, F., Perignon, Y., and Bianchini, A.: Derivation of Met-Ocean Conditions for the Simulation of Floating Wind Turbines:
842 a European case study, *J. Phys.: Conf. Ser.*, 2385, 012117, <https://doi.org/10.1088/1742-6596/2385/1/012117>, 2022c.
- 843 Papi, F., Bianchini, A., Troise, G., Mirra, G., Marten, D., Saverin, J., Behrens de Luna, R., Ducasse, M.-L., and Honnet, J.:
844 Deliverable 2.4 Full report on the estimated reduction of uncertainty in comparison to the state-of-the-art codes OpenFAST
845 and DeepLines Wind, 2023.

- 846 Perez-Becker, S., Papi, F., Saverin, J., Marten, D., Bianchini, A., and Paschereit, C. O.: Is the Blade Element Momentum
847 theory overestimating wind turbine loads? – An aeroelastic comparison between OpenFAST’s AeroDyn and QBlade’s Lifting-
848 Line Free Vortex Wake method, *Wind Energ. Sci.*, 5, 721–743, <https://doi.org/10.5194/wes-5-721-2020>, 2020.
- 849 Perez-Becker, S., Saverin, J., Behrens de Luna, R., Papi, F., Combreau, C., Ducasse, M.-L., Marten, D., and Bianchini, A.:
850 Deliverable 2.2 - Validation Report of QBlade-Ocean, 2022.
- 851 Robertson, A. and Jonkman, J.: Loads Analysis of Several Offshore Floating Wind Turbine Concepts, International Society of
852 Offshore and Polar Engineers 2011 Conference, Maui, Hawaii, 10, 2011.
- 853 Robertson, A., Jonkman, J., Masciola, M., Song, H., Goupee, A., Coulling, A., and Luan, C.: Definition of the Semisubmersible
854 Floating System for Phase II of OC4, <https://doi.org/10.2172/1155123>, 2014a.
- 855 Robertson, A., Jonkman, J., Vorpahl, F., Popko, W., Qvist, J., Frøyd, L., Chen, X., Azcona, J., Uzunoglu, E., Guedes Soares,
856 C., Luan, C., Yutong, H., Pengcheng, F., Yde, A., Larsen, T., Nichols, J., Buils, R., Lei, L., Nygaard, T. A., Manolas, D.,
857 Heege, A., Vatne, S. R., Ormberg, H., Duarte, T., Godreau, C., Hansen, H. F., Nielsen, A. W., Riber, H., Le Cunff, C., Beyer,
858 F., Yamaguchi, A., Jung, K. J., Shin, H., Shi, W., Park, H., Alves, M., and Guérinel, M.: Offshore Code Comparison
859 Collaboration Continuation Within IEA Wind Task 30: Phase II Results Regarding a Floating Semisubmersible Wind System,
860 in: Volume 9B: Ocean Renewable Energy, ASME 2014 33rd International Conference on Ocean, Offshore and Arctic
861 Engineering, San Francisco, California, USA, V09BT09A012, <https://doi.org/10.1115/OMAE2014-24040>, 2014b.
- 862 Robertson, A. N., Wendt, F., Jonkman, J. M., Popko, W., Dagher, H., Gueydon, S., Qvist, J., Vittori, F., Azcona, J., Uzunoglu,
863 E., Soares, C. G., Harries, R., Yde, A., Galinos, C., Hermans, K., de Vaal, J. B., Bozonnet, P., Bouy, L., Bayati, I., Bergua, R.,
864 Galvan, J., Mendikoa, I., Sanchez, C. B., Shin, H., Oh, S., Molins, C., and Debruyne, Y.: OC5 Project Phase II: Validation of
865 Global Loads of the DeepCwind Floating Semisubmersible Wind Turbine, *Energy Procedia*, 137, 38–57,
866 <https://doi.org/10.1016/j.egypro.2017.10.333>, 2017.
- 867 Robertson, A. N., Gueydon, S., Bachynski, E., Wang, L., Jonkman, J., Alarcón, D., Amet, E., Beardsell, A., Bonnet, P., Boudet,
868 B., Brun, C., Chen, Z., Féron, M., Forbush, D., Galinos, C., Galvan, J., Gilbert, P., Gómez, J., Harnois, V., Haudin, F., Hu, Z.,
869 Dreff, J. L., Leimeister, M., Lemmer, F., Li, H., Mckinnon, G., Mendikoa, I., Moghtadaei, A., Netzband, S., Oh, S., Pegalajar-
870 Jurado, A., Nguyen, M. Q., Ruehl, K., Schünemann, P., Shi, W., Shin, H., Si, Y., Surmont, F., Trubat, P., Qvist, J., and
871 Wohlfahrt-Laymann, S.: OC6 Phase I: Investigating the underprediction of low-frequency hydrodynamic loads and responses
872 of a floating wind turbine, *J. Phys.: Conf. Ser.*, 1618, 032033, <https://doi.org/10.1088/1742-6596/1618/3/032033>, 2020.
- 873 Stewart, G. M.: Design Load Analysis of Two Floating Offshore Wind Turbine Concepts, University of Massachusetts
874 Amherst, <https://doi.org/10.7275/7627466.0>, 2016.
- 875 Valamanesh, V., Myers, A. T., and Arwade, S. R.: Multivariate analysis of extreme metocean conditions for offshore wind
876 turbines, *Structural Safety*, 55, 60–69, <https://doi.org/10.1016/j.strusafe.2015.03.002>, 2015.
- 877 Van Garrel, A.: Development of a wind turbine aerodynamics simulation module, 2003.
- 878 Vigarà, F., Cerdán, L., Durán, R., Muñoz, S., Lynch, M., Doole, S., Molins, C., Trubat, P., and Gunache, R.: COREWIND
879 D1.2 Design Basis, , <https://doi.org/10.5281/zenodo.4518828>, 2020.
- 880 Wang, L., Robertson, A., Jonkman, J., and Yu, Y.-H.: OC6 phase I: Improvements to the OpenFAST predictions of nonlinear,
881 low-frequency responses of a floating offshore wind turbine platform, *Renewable Energy*, 187,
882 <https://doi.org/10.1016/j.renene.2022.01.053>, 2022.

883 Yu, W., Müller, K., and Lemmer, F.: D4.2 Public Definition of the Two LIFES50+ 10MW Floater Concepts, University of
884 Stuttgart, 2018.

885

887



888

889 **Figure A1: Selection of ultimate loads (minimum) recorded in the three simulation codes. (a) DTU 10MW Hexafloat, (b) DTU 10MW**
 890 **Softwind and (c) NREL 5MW OC4.**

891